Monthly Notices
of the
ROYAL ASTRONOMICAL SOCIETY

MNRAS **488,** 2743–2766 (2019)
Advance Access publication 2019 June 12

doi:10.1093/mnras/stz1624

The hidden giant: discovery of an enormous Galactic dwarf satellite in *Gaia* DR2

G. Torrealba [1]★ V. Belokurov [2,3] S. E. Koposov [2,4] T. S. Li,[5,6] M. G. Walker,[4] J. L. Sanders [2] A. Geringer-Sameth,[7] D. B. Zucker,[8,9] K. Kuehn,[10] N. W. Evans[2] and W. Dehnen [11,12]

[1]*Institute of Astronomy and Astrophysics, Academia Sinica, P.O. Box 23-141, Taipei 10617, Taiwan*
[2]*Institute of Astronomy, University of Cambridge, Madingley Road, Cambridge CB3 0HA, UK*
[3]*Center for Computational Astrophysics, Flatiron Institute, 162 5th Avenue, New York, NY 10010, USA*
[4]*McWilliams Center for Cosmology, Department of Physics, Carnegie Mellon University, 5000 Forbes Avenue, Pittsburgh, PA 15213, USA*
[5]*Fermi National Accelerator Laboratory, P.O. Box 500, Batavia, IL 60510, USA*
[6]*Kavli Institute for Cosmological Physics, University of Chicago, Chicago, IL 60637, USA*
[7]*Department of Physics, Imperial College London, Blackett Laboratory, Prince Consort Road, London SW7 2AZ, UK*
[8]*Department of Physics & Astronomy, Macquarie University, Sydney, NSW 2109, Australia*
[9]*Macquarie University Research Centre for Astronomy, Astrophysics and Astrophotonics, Macquarie University, Sydney, NSW 2109, Australia*
[10]*Australian Astronomical Optics, Macquarie University, North Ryde, NSW 2113, Australia*
[11]*Department of Physics & Astronomy, University of Leicester, University Road, Leicester LE1 7RH, UK*
[12]*Sternwarte der Ludwig-Maximilians-Universität, Scheinerstrasse 1, München D-81679, Germany*

Accepted 2019 June 10. Received 2019 June 8; in original form 2018 November 9

ABSTRACT

We report the discovery of a Milky Way satellite in the constellation of Antlia. The Antlia 2 dwarf galaxy is located behind the Galactic disc at a latitude of $b \sim 11^\circ$ and spans 1.26°, which corresponds to ∼2.9 kpc at its distance of 130 kpc. While similar in spatial extent to the Large Magellanic Cloud, Antlia 2 is orders of magnitude fainter at $M_V = -9$ mag, making it by far the lowest surface brightness system known (at ∼31.9 mag arcsec^{-2}), ∼100 times more diffuse than the so-called ultra diffuse galaxies. The satellite was identified using a combination of astrometry, photometry, and variability data from *Gaia* Data Release 2, and its nature confirmed with deep archival DECam imaging, which revealed a conspicuous BHB signal. We have also obtained follow-up spectroscopy using AAOmega on the AAT, identifying 159 member stars, and we used them to measure the dwarf's systemic velocity, 290.9 ± 0.5 km s^{-1}, its velocity dispersion, 5.7 ± 1.1 km s^{-1}, and mean metallicity, [Fe/H] = −1.4. From these properties we conclude that Antlia 2 inhabits one of the least dense dark matter (DM) haloes probed to date. Dynamical modelling and tidal-disruption simulations suggest that a combination of a cored DM profile and strong tidal stripping may explain the observed properties of this satellite. The origin of this core may be consistent with aggressive feedback, or may even require alternatives to cold dark matter (such as ultra-light bosons).

Key words: Galaxy: halo – galaxies: dwarf – galaxies: individual: Antlia 2 Dwarf.

1 INTRODUCTION

While the population of Galactic low-luminosity dwarf satellites may have been sculpted by a number of yet-unconstrained physical processes such as cosmic reionization (see e.g. Bose, Deason & Frenk 2018) and stellar feedback (see e.g. Fitts et al. 2017), the total number of bright satellites depends strongly only on the mass of the host galaxy, and thus can be predicted more robustly. According to, e.g. Garrison-Kimmel et al. (2018), in the Milky Way today there may remain between 1 and 3 undetected satellites with stellar masses $M_* > 10^5$ M$_\odot$. An obvious place where such a satellite might reside is the so-called Zone of Avoidance (ZOA, see e.g. Shapley 1961; Kraan-Korteweg & Lahav 2000), a portion of the sky at low Galactic latitude, affected by elevated dust extinction and a high density of intervening disc stars. The paucity of Galactic dwarf satellites in this region was already apparent in the catalogue of Mateo (1998) and has remained mostly unchanged until the present day (see McConnachie 2012).

★ E-mail: gtorrealba@asiaa.sinica.edu.tw

Until recently, little had been done to search for Galactic satellites in the ZOA for obvious reasons. First, the region within $|b| < 15^{\circ}$ did not have contiguous coverage of uniform quality. Secondly, the foreground disc populations at these latitudes suffer large amounts of differential reddening, thus displaying complicated and rapidly varying behaviour in colour–magnitude space. However, today, thanks to data from ESA's *Gaia* space observatory (Gaia Collaboration 2016a), both of the limiting factors above can be easily mitigated. For example, Koposov, Belokurov & Torrealba (2017) used *Gaia* Data Release 1 (GDR1, Gaia Collaboration 2016b) to discover two new star clusters, both with $|b| < 10^{\circ}$. They also highlighted *Gaia*'s potential to detect low-luminosity satellites with surface brightness levels similar to or fainter than those achieved by much deeper sky surveys (see also Antoja et al. 2015). As explained in Koposov et al. (2017), what *Gaia* lacks in photometric depth, it makes up in star/galaxy separation and artefact rejection. Torrealba, Belokurov & Koposov (2019) continued to mine the GDR1 data to find an additional four star clusters all within 10° of the Galactic plane. Impressively, the two satellite searches above had to rely solely on *Gaia* star counts, as no proper motion, colour, or variability information was available as part of GDR1 for the majority of sources.

In this paper, we use *Gaia* Data Release 2 (GDR2, Gaia Collaboration 2018a) to discover and analyse a new dwarf satellite galaxy orbiting the Milky Way. The discovery was made at the Flatiron Gaia Sprint 2018. We are able to exploit not only the positions of stars detected on-board *Gaia*, but also their colours, proper motions, and parallaxes. Additionally, we take advantage of the large database of variable stars identified by *Gaia* and supplied as part of GDR2 (see Gaia Collaboration 2019; Holl et al. 2018), in particular, the RR Lyrae (RRL) stars (see Clementini et al. 2019). Our search represents the first 'quick and dirty' pass through GDR2 data in search of Galactic satellites, and relies on the fact that all of the currently known Milky Way dwarfs contain at least one RRL star (see Sesar et al. 2014; Baker & Willman 2015). We also make use of GDR2 parallax measurements to remove the bulk of the foreground disc population, as suggested in Antoja et al. (2015) and implemented in e.g. Belokurov & Erkal (2019).

The combined use of *Gaia*'s photometric, astrometric, and variability information allows one to reach levels of surface brightness below those previously attainable with photometry alone. The extension of the current Galactic dwarf population to yet fainter systems has been expected, given that many of the recent satellite discoveries pile up around the edge of detectability, hovering in the size–luminosity plane around a surface brightness of ∼30 mag arcsec^{-2} (see e.g. Torrealba et al. 2016b). In other words, it appeared to be only a matter of time until the ultra-faint galaxy regime would segue into 'stealth' galaxies, with objects at even lower total luminosities but comparable sizes (see Bullock et al. 2010). Perhaps even more surprising is the recent detection of a galaxy – the Crater 2 dwarf – with an extremely low surface brightness, but at a total luminosity close to the classical dwarf regime, i.e. $L \sim 10^5\,L_{\odot}$ (see Torrealba et al. 2016a). Cra 2 occupies a poorly explored region of structural parameter space, where ordinary stellar masses meet extraordinarily large sizes, resulting in record-breaking low surface brightness levels (∼30.6 mag arcsec^2) – a regime not predicted to be populated by earlier extrapolations (e.g. Bullock et al. 2010). Stranger still, Cra 2 appears to be not only one of the largest Milky Way dwarfs, but also one of its coldest (in terms of the stellar velocity dispersion, see Caldwell et al. 2017). Of the plausible mechanisms capable of dialing down both the satellite's surface brightness and velocity dispersion, tidal stripping immediately comes to mind (see e.g. Peñarrubia, Navarro & McConnachie 2008b). But, as shown by Sanders, Evans & Dehnen (2018), it is rather difficult to produce a diffuse and cold system such as Cra 2 only via the tidal stripping of a stellar system embedded in a cuspy (see e.g. Dubinski & Carlberg 1991; Navarro, Frenk & White 1996b) dark matter halo.

As Sanders et al. (2018) convincingly demonstrate, however, if Cra 2 were embedded in a cored (i.e. shallower inner density – see e.g. Moore 1994; Navarro, Eke & Frenk 1996a) dark matter (DM) halo, reproducing its present structural and kinematic properties would be much easier. Such cores can naturally arise if the physics of the DM particle is altered (see e.g. Hogan & Dalcanton 2000; Hu, Barkana & Gruzinov 2000; Peebles 2000; Spergel & Steinhardt 2000), but even within cold DM cosmology the inner density profiles of galaxy-hosting haloes can be substantially flattened via strong stellar feedback (e.g. El-Zant, Shlosman & Hoffman 2001; Gnedin et al. 2004; Read & Gilmore 2005; Mashchenko, Wadsley & Couchman 2008; Pontzen & Governato 2012). While the study of the effects of supernova feedback on the structure of galaxies currently remains firmly in the realm of 'sub-grid' physics, many simulations show that the changes induced are not limited to the dwarf's central regions. Powerful bursty gaseous outflows have been shown to be able to 'drag' many of the constituent stars to much larger radii overall, thus creating noticeably diffuse dwarf galaxies (see e.g. El-Badry et al. 2016; Di Cintio et al. 2017; Chan et al. 2018).

This paper is organized as follows. Section 2 gives the details of the search algorithm and archival imaging processing; it also describes the modelling of the structural properties of the system and the estimates of its distance. Section 3 presents the analysis of the spectroscopic follow-up as well as the details of the kinematic modelling. Section 4 compares the new satellite to the population of previously known Milky Way dwarfs, and gives an interpretation of its DM properties. Concluding remarks can be found in Section 5.

2 THE HIDDEN GIANT

2.1 Discovery in *Gaia* DR2

Gaia DR2 boasts many unique properties that allow one to study the outskirts of the Milky Way as never before. Perhaps the most valuable of these is the wealth of high-quality all-sky proper motion (PM) information. *Gaia*'s astrometry makes it possible to filter out nearby contaminating populations, revealing the distant halo behind them. Halo studies are further boosted by the use of *Gaia*'s variable star data, specifically the RRL catalogue (see Holl et al. 2018, for details), which provides precise distances out to (and slightly beyond) ∼100 kpc. RRLs are the archetypal old, metal-poor stars, and hence a perfect tracer of the Milky Way's halo, including the dwarf satellite galaxies residing in it. Indeed, all but one dSph (Carina III, see Torrealba et al. 2018, for further discussion) that have been studied so far contain at least one RRL (Baker & Willman 2015). This makes searches for stellar systems co-distant with RRLs a plausible means to probe for low surface brightness Milky Way halo sub-structure (see e.g. Sesar et al. 2014; Baker & Willman 2015).

In this work, we combine the use of both *Gaia*'s astrometry and its RRL catalogues to look for previously unknown MW satellites. We use a clean sample of RRLs from the *gaiadr2.vari_rrlyrae* table provided by *Gaia* DR2, and look for overdensities of stars with the same proper motions as the RRL considered. Specifically, we first

estimate the RRL distance modulus as

$$D_{\rm h} = \langle G \rangle - 3.1 \frac{A_G}{A_V} E(B-V) - 0.5, \quad (1)$$

where $\langle G \rangle$ is the intensity-averaged G magnitude, $E(B-V)$ is taken from the Schlegel, Finkbeiner & Davis (1998) extinction map, and $A_G/A_V = 0.859$ is the extinction coefficient for the *Gaia* G band (Malhan, Ibata & Martin 2018)[1]. For simplicity we assumed an absolute magnitude for the RRL of 0.5 (but see Iorio & Belokurov 2019). Then, we cleaned up the RRL sample by removing stars with *astrometric_excess_noise* larger than 1, and reduced the sample to search only around stars that have $D_{\rm h} > 50$ and that are at least 15° away from the LMC and SMC. The stars selected for the overdensity search were taken in a 2° radius from the central RRL. Only stars with PMs consistent – within the uncertainties – with the central RRL PM were considered. Additionally, we removed stars with low heliocentric distances by applying a cut on parallax of $\varpi > 0.5$.

Specifically, the overdensity search was performed as follows. We counted the number of the previously selected stars within circular apertures ranging in radius from 1 to 30 arcmin (from the central RRL), and compared these to the foreground, which was estimated in the area between 1° and 2° away from the RRL star. If any of the samples exceeded by more than 2σ the expected foreground number, we flagged the trial RRL as a possible tracer of a stellar system. By plotting the flagged RRL in the sky – together with the known satellite galaxies and the globular clusters – we immediately noticed that three flagged RRL with distances between 55 and 90 kpc were bunching up in a small region of the sky where no known stellar system was present. A closer inspection revealed that the RRLs shared the same PM; moreover the PM-filtered stars in the region had a conspicuous signal both in the CMD and on the sky, as seen in Fig. 1. More precisely, the left-hand panel of the figure shows the spatial distribution of the stars selected using the PM and the CMD cuts. Here a large stellar overdensity spanning more than 1° on the sky is visible. The middle panel gives the CMD density of stars within the half-light radius (red dashed line in left-hand panel, see Section 2.2 for its definition), and after applying the PM cut. A broad Red Giant Branch (RGB) at a distance of $\gtrsim$100 kpc can be easily discerned. The red polygon indicates the CMD mask used for the selection, which was empirically defined based on the RGB feature. Finally, the right-hand panel of the figure demonstrates the PM density of stellar sources within the half-light radius and inside the CMD mask shown in the middle panel. A tight overdensity is noticeable around $\mu_\alpha \sim 0$ and $\mu_\delta \sim 0$. The red ellipse outlines the PM selection boundary, as defined in Section 2.2. Based only on the approximate distance, the size, and the breadth of the RGB we can safely conclude that the newly found object is a dwarf galaxy satellite of the Milky Way. This hypothesis is further tested and confirmed below. As the dwarf is discovered in the constellation of Antlia (or the Pump), we have given it the name Antlia 2 (or Ant 2). Note that Ant 2's neighbour on the sky, the previously found Antlia dwarf, is a transition-type dwarf (i.e. a galaxy with properties similar to both dwarf spheroidals and dwarf irregulars) on the outskirts of the Local Group (i.e. beyond 1 Mpc, see Whiting, Irwin & Hau 1997).

[1]The coefficients for the B_P and R_P used to create fig. 1 are $A_{B_P}/A_V = 1.068$ and $A_{R_P}/A_V = 0.652$ (Malhan et al. 2018). Note, however, that reddening corrections have a typical uncertainty of around 10 per cent, owing to both the scatter in the fit of the extinction coefficient, and the variability of R_V (see appendix B of Schlegel et al. 1998, for further details).

2.2 Photometric modelling

2.2.1 Deep DECam imaging data

To better characterize the new object, we checked whether any deeper photometric data were available. In this region, photometry with partial coverage was found in the NOAO source catalogue (Nidever et al. 2018); additionally several unprocessed images were available from the NOAO archive. We searched for DECam data in the g and r bands in a 100 deg^2 region around (RA, Dec.) = 144.1558, −37.075 09, and retrieved the *instcal* and weight frames provided by NOAO. Most of the area is covered with images from two Programs, namely 2017A-0260 (the BLISS survey) and 2015A-0609, but we also downloaded images from Programs 2013B-0440 and 2014B-0440, although these latter two only added three fields in total in the outskirts of the region.

Photometry was carried out using the standard SExtractor + psfex combination (see e.g. Koposov et al. 2015a, for a similar approach). We kept the configuration standard, except for a smaller detection threshold, which was set to 1, and a more flexible deblending threshold. The photometric zero-point was calibrated against the ninth APASS data release (Henden et al. 2015) as the median magnitude offset on a per-chip basis. If fewer than 10 stars were available on a chip, then the field median offset was used instead. We finalized the calibration with a global correction. This procedure gave a photometric zero-point precision of 0.078 in g band and 0.075 in r band. To generate the final band-merged source catalogues, we first removed duplicates using a matching radius of 1 arcsec, and then cross-matched the g- and r-band lists with the same matching radius, only keeping objects that had measurements in both bands. We also cross-matched the resulting catalogue with the *Gaia* DR2 source list – also using a 1 arcsec radius – to complement the DECam photometry with PM information where available. The final catalogue covers ∼88 deg^2, of which ∼65 come from Program 2017A-0260 with a limiting magnitude of ∼23.2. The remaining 23 deg^2 are from 2015A-0609 and have a limiting magnitude of 22.2 (both before extinction correction). The extinction correction was done using the dust maps from Schlegel et al. (1998) and the extinction coefficients from Schlafly & Finkbeiner (2011). Note that Antlia 2 is in a region of high extinction, with ∼0.6 mag of extinction in g and ∼0.4 mag in r, which adds ∼0.05 mag to the uncertainty if one considers the 10 per cent uncertainty on the reddening correction (Schlegel et al. 1998). Throughout the paper we usually refer to the extinction-corrected magnitudes, which are labelled with the subscript 0. Finally, likely stars are separated from the likely galaxies by removing objects with *SPREAD_MODEL* greater than 0.003 + *SPREADERR_MODEL* in both g and r bands.

Fig. 2 shows the area of the sky around Ant 2 in the archival DECam data. From left to right, we present the stellar density distribution on the sky, the density of stars in CMD space, and density of stars in PM space. The top panels show all stars in our DECam catalogues, while the bottom panels show only the selected candidate Ant 2 member stars. Note that, although we have photometric catalogues that reach down to $r_0 \sim 23.2$, we only use stars cross-matched to the GDR2 catalogues due to the need for PMs for our analysis. The GDR2's PMs are only available – with high completeness – down to 20.4 in g_0, and to 20 in r_0. As the top row of the figure demonstrates, the object is essentially invisible when no filters are applied. Given the complex, overpowering stellar foreground population, we decided to characterize the object independently in the three parameter spaces.

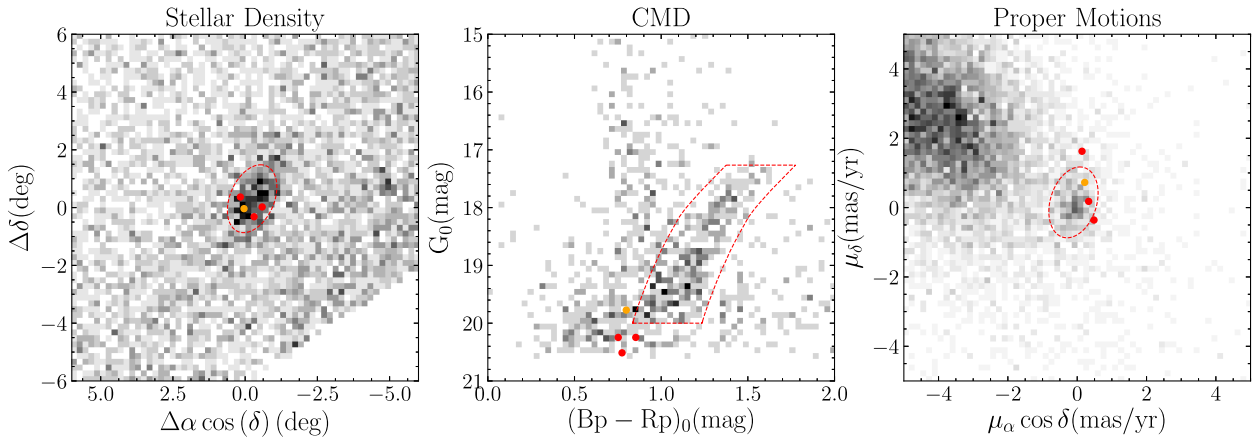

Figure 1. Discovery of Antlia 2 in the *Gaia* DR2 data. *Left:* Proper motion and CMD-filtered stars in a ∼100 deg^2 region around Ant 2. The gigantic elongated overdensity in the centre is easily visible once the proper motion, the CMD and the parallax cuts (see main text) are applied. Red and orange filled circles, for stars with heliocentric distances larger than 70 kpc, and between 55 and 70 kpc, respectively, show the position of the four RRL that we originally used to find Ant 2 (see Section 2.3 and Fig. 3 for more details). *Middle:* CMD of the *Gaia* DR2 stars within the half-light radius of Ant 2 filtered by proper motion, featuring an obvious RGB at a distance of ∼130 kpc. *Right:* Stellar PMs within the half-light radius selected using their position on the CMD, highlighting a clear overdensity around 0. In each panel, red dashed lines show the selection boundaries used to pick out the likely satellite members.

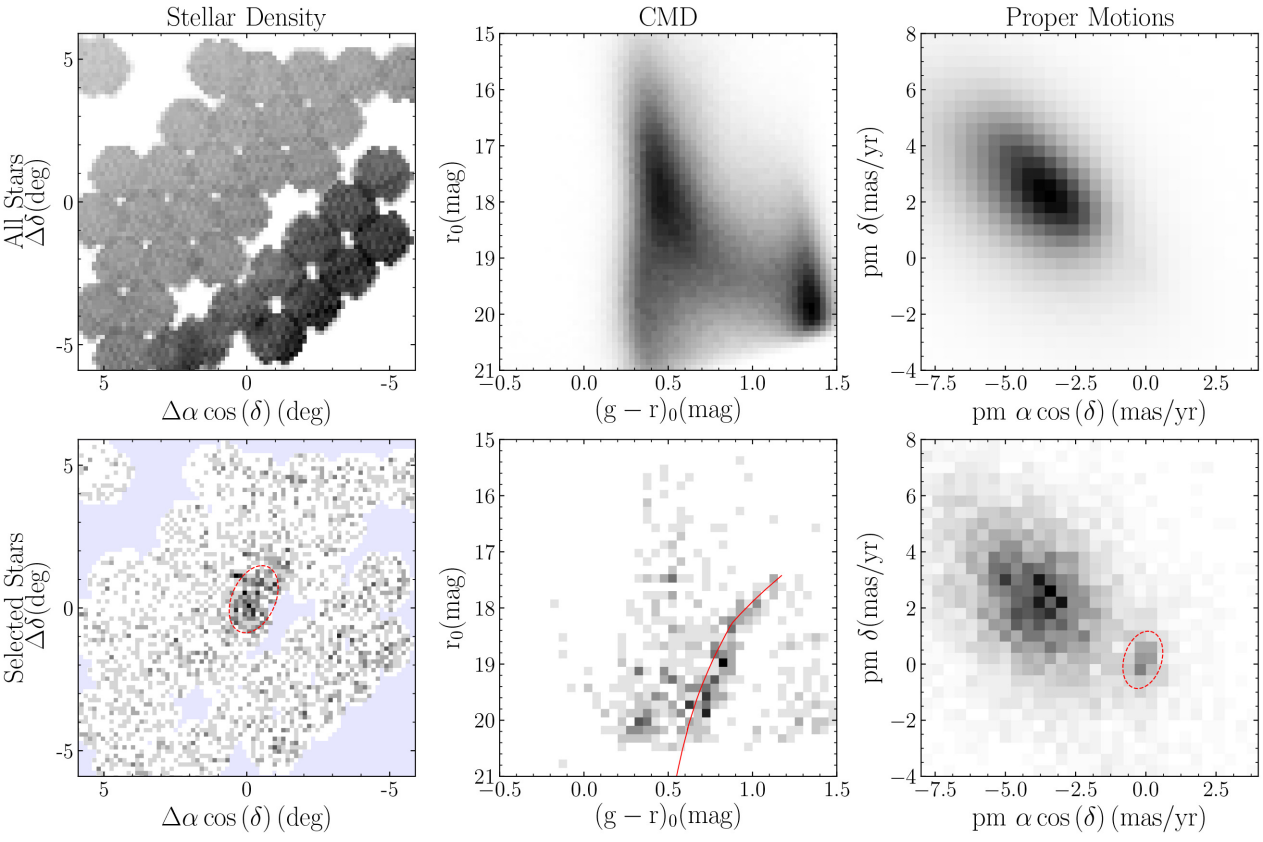

Figure 2. DECam view of Antlia 2. Stars in a ∼100 deg^2 region centred on the dwarf with available PMs from GDR2 are shown. The top row gives the properties of all stars in this portion of the sky, while the bottom panels illustrate the properties of the likely Ant 2 members. *Left:* Distribution of the stellar density on the sky. The red ellipse corresponds to the half-light radius of the best-fitting model ($r_h = 1.26^\circ$), and marks the boundary used for the spatial selection. The blue shaded regions in the lower panel indicate the areas without DECam data. *Middle:* Hess diagram, i.e. stellar density in the CMD. The red line corresponds to the best-fitting isochrone with log age $= 10$ and [Fe/H] $= -1.5$. *Right:* Stellar density in proper motion space. The red ellipse marks the PM selection boundary. Being very close to the Galactic disc ($b \sim 11^\circ$), the region around Ant 2 is heavily dominated by the MW foreground. None the less, after applying all of the selection cuts (including the parallax, see main text), Ant 2's signal appears conspicuous in all three parameter spaces.

We start by modelling the distribution of the dwarf's PMs, since in this space the satellite's signal can be most easily differentiated from that of the foreground. To proceed, we apply the spatial and the CMD cuts based on the signals seen in the bottom row of Fig. 2. Then we model the resulting PM distribution as a mixture of three Gaussians, two representing the foreground and one for Ant 2 itself. The bottom right panel of Fig. 2 gives the density distribution of the CMD + spatially selected stars along with a contour corresponding to the best-fitting Gaussian shown in a red dashed line. The resulting Gaussian profile, centred at $(\mathrm{pm}\,\alpha\cos(\delta)\,,\mathrm{pm}\,\delta) = (-0.1, 0.15)$, provides a good description of the PM 'blob' seen in the figure. The red dashed contour shown in the right-hand panel of Fig. 1 and in the bottom right panel of Fig. 2 is the mask we apply to select stars that belong to Antlia 2 based on PMs.

Next, we analyse the observed stellar spatial distribution using the full 88 deg^2 of DECam imaging available. We first apply the PM and the CMD cuts, and then model the resulting distribution as a mixture of a planar foreground and a Plummer profile, following the same procedure as described in, e.g. Torrealba et al. (2019). In order to obtain robust and useful uncertainties for the parameters of our spatial model, we sample the likelihood using the ensemble sampler (Goodman & Weare 2010) implemented in the EMCEE package (Foreman-Mackey et al. 2013). We chose flat priors for all parameters except for the dwarf's size, which uses the Jeffreys prior, i.e. $1/a$, where a is the size parameter. The best-fitting parameters and their uncertainties are estimated from the marginalized posterior distributions corresponding to the 15.9 per cent, 50 per cent, and 84.1 per cent. The half-light radius of the best-fitting model is shown as the red ellipse in the bottom left panel of Fig. 2, corresponding to a whopping $r_\mathrm{h} = 1.26 \pm 0.12$ deg. The Ant 2 dwarf's angular extent is similar to that of the SMC (1.25 deg, Torrealba et al. 2016a), with only the LMC (2.5 deg, Torrealba et al. 2016a) and Sagittarius (5.7 deg, McConnachie 2012) being larger in the sky. Curiously, this is almost three times larger than the next largest known satellites, Cra 2 and BooIII, both with $r_\mathrm{h} \sim 0.5$ deg (Grillmair 2009; Torrealba et al. 2016a). Located at ∼130 kpc (see Section 2.3 for details), this angular extent translates to $\sim 2.9 \pm 0.3$ kpc, which is equal in size to the LMC! A summary of the relevant physical parameters measured above is presented in Table 1.

Finally, we model the stellar distribution in CMD space using Padova isochrones (Bressan et al. 2012) for the satellite's stars and an empirically estimated foreground. In line with previous steps, we first apply a spatial cut, using the best-fitting structural model, as well as a PM cut based on the constraint derived above. Additionally, we fix the distance modulus to the value obtained by fitting the satellite BHB candidates (see Section 2.3 for details); more precisely we use $m - M = 20.6$, and we set up a magnitude limit of 20 in r_0 and 20.4 in g_0, corresponding to the range within which all stars have their PMs measured by *Gaia*. The isochrone models are built on a colour–magnitude grid by convolving the expected number of stars along the isochrone with the photometric uncertainties. We also convolve the maps with a Gaussian with $\sigma = 0.2$ mag along the magnitude component to account for the observed spread in distance modulus, which corresponds to the full width of the BHB sequence (see the middle panel of Fig. 3). The modelling is performed only between $0.5 < (g - r)_0 < 1.5$, since this is the region where the RGB, the only easily discernible CMD feature, is located. To create the foreground model, we make a density map of the stars in the same part of the sky, but removing the stars with the PM of Ant 2. Finally, we pick isochrones on a grid of logarithmic ages between 9.6 and 10.1 and metallicities between −2.1 and −0.8 and measure the likelihood of the data given each isochrone. For each isochrone, the only parameter we fit is the ratio of the foreground stars to the satellite's. The best-fitting model obtained is that with log(age) = 10.0 and [Fe/H] = −1.5. The best-fitting isochrone along with the PM and spatial filtered CMD is shown in the middle panel of Fig. 2. Note that the good fit of the RGB at the given distance modulus provides an independent confirmation of the distance to Ant 2. Using the above CMD model, specifically the ratio of satellite members to background/foreground, and the spatial model to account for chip-gaps, we can infer the total number of Ant 2's stars above the limiting magnitude to be $N = 246 \pm 30$. Given that the catalogue is close to 100 per cent completeness for $g_0 < 20.4$, we can combine the total number of stars with the best-fit isochrone, which assumes a Chabrier IMF (Chabrier 2003), to estimate the absolute magnitude of Ant 2 as $M_V = -9.03 \pm 0.15$, which is equivalent to a stellar mass of $M_\star = 2.5 \times 10^{0.4(4.83-M_v)} = (8.8 \pm 1.2) \times 10^5\,\mathrm{M}_\odot$.

Table 1. Properties of the Antlia 2 dwarf.

Property	Antlia 2 dwarf	Unit
α(J2000)	143.8868 ± 0.05	deg
δ(J2000)	− 36.7673 ± 0.10	deg
l	264.8955 ± 0.05	deg
b	11.2479 ± 0.10	deg
$(m - M)$	20.6 ± 0.11	mag
$D_\odot$	132 ± 6	kpc
r_h	1.27 ± 0.12	deg
r_h	2920 ± 311	pc
$1 - b/a$	0.38 ± 0.08	
PA	156 ± 6	deg
M_V	− 9.03 ± 0.15	mag
$\langle\mu\rangle(r < r_\mathrm{h})$	31.9 ± 0.3	mag arcsec^{-2}
[Fe/H]	− 1.36 ± 0.04	dex
$\sigma_\mathrm{[Fe/H]}$	0.57 ± 0.03	dex
rv_helio	290.7 ± 0.5	km s^{-1}
rv_gsr	64.3 ± 0.5[b]	km s^{-1}
σ_{rv}	5.71 ± 1.08	km s^{-1}
$\mu_\alpha \cos\delta$	− 0.095 ± 0.018[a]	mas yr^{-1}
μ_δ	0.058 ± 0.024[a]	mas yr^{-1}
$M(r < r_\mathrm{h})$	5.5 ± 2.2	10^7 M$_\odot$
$M(r < 1.8r_\mathrm{h})$	13.7 ± 5.4	10^7 M$_\odot$
$M_\star$	8.8 ± 1.2	10^5 M$_\odot$
M/L_V	315 ± 130	M$_\odot$/L$_\odot$

[a]Does not consider systematic uncertainties (see text).
[b]Does not consider LSR uncertainties.

2.3 Horizontal branch and distance

If no PM cut is applied, it is very difficult to see the RGB feature in the CMD, but it is still possible to see a strong BHB sequence at $r_0 \sim 21.2$. This is illustrated in the left-hand panel of Fig. 3, in which we show the blue part of the differential Hess diagram between the stars within the half-light radius of Ant 2 and those in the foreground. The sample shown comes from the region where the limiting magnitude in the r band is 23.2. The red line indicates the BHB ridge-line from Deason et al. (2011) at the distance modulus of 20.6. This is the best-fitting value obtained by measuring the distance modulus of all stars within the dashed red box, assuming they are drawn from the above ridge-line. The distribution of the observed distance moduli is shown in the middle panel of the figure, along with a two-Gaussian model, where one component describes the peak associated with Antlia 2 BHBs, and the other models the foreground. The main peak at ∼20.6 is well fit by the Gaussian

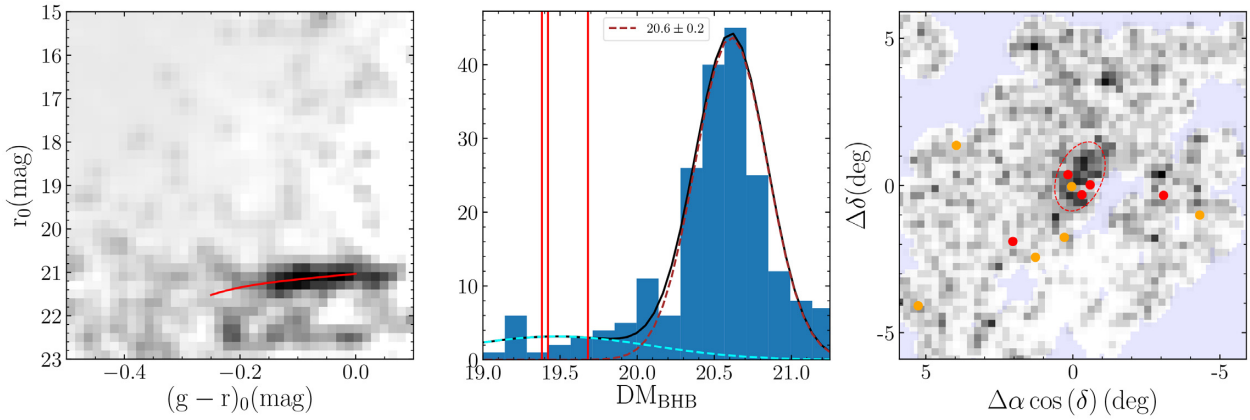

Figure 3. BHBs and RRL stars in Antlia 2. *Left:* DECam Hess difference (difference of CMD densities) of the stars within the Ant 2's half-light radius and the foreground, zoomed in on the BHB region. The red line shows the BHB ridge-line as given in Deason, Belokurov & Evans (2011) at the best-fitting distance modulus. *Middle:* Distribution of the distance moduli of the selected BHB candidates, along with the best-fitting two-Gaussian plus a flat background model. The vertical lines mark the distance moduli of the four RRL stars within the half-light radius of the satellite. *Right:* On-sky density distribution of the BHB candidates. RRL stars with heliocentric distances larger than 70 kpc are shown in red, stars with distances between 55 and 70 kpc are shown in orange.

with a width of 0.2 mag. Note however that the formal uncertainty on the centre of the Gaussian is only 0.02. Nevertheless there is a systematic uncertainty of ∼0.1 mag in the absolute magnitude of the BHB ridge line itself (Deason et al. 2011, Fig. 4) which sets the uncertainty in our DM measurement to 0.1.

This translates into a distance of 132 ± 6 kpc. The red vertical lines in the middle panel of Fig. 3 show the distance moduli of the three RRL originally found around Ant 2. Clearly, these variable stars – while located far in the halo – appear to be positioned well in front of the dwarf along the line of sight. We speculate that this handful of RRL detected by *Gaia* may be on the near side of an extended cloud of tidal debris (see Section 4 for details) emanating from the dwarf. Note, however, that all three RRL lie close to the limiting magnitude of Gaia, therefore their median flux estimate may be biased high and, correspondingly, their distances biased low. Given its luminosity, Ant 2 is likely to host many tens of RRL, similar to, e.g. its close analogue, Crater 2 (see Joo et al. 2018; Monelli et al. 2018). At the distance of the main body of the dwarf, RRL would be too faint for *Gaia* but should be detectable with deeper follow-up imaging. The distribution of the DECaM BHBs, along with the RRLs with distances larger than 55 kpc, is shown in the right-hand panel of Fig. 3. An obvious BHB overdensity with a shape very similar to that of the RGB stars is visible at the position of Antlia 2, further confirming that the BHB and the RGB features are correlated.

3 SPECTROSCOPIC FOLLOW-UP

Immediately after the object's discovery at the Flatiron Gaia Sprint, we sought to obtain spectroscopic follow up of some of Ant 2's RGB members. The night of 2018 June 24 we obtained service mode observations of targets in the field of Ant 2 with the 2dF + AAOmega Spectrograph (Sharp et al. 2006) on the 3.9 m Anglo-Australian Telescope. The data consist of 3 × 30 min exposures taken with an average seeing of 1.4 arcsec, over an airmass range of 1.4–2 and at a moon distance of ∼80° from the full moon. We used 580V (R ∼1300) and 1700D (R ∼10 000) gratings in the blue and red channels, respectively. Because of the bright moon conditions during observations, the signal-to-noise of the blue spectra taken with the 580V grating was low, and hence we only used the red 1700D spectra – covering the wavelength range between 8450 and 9000 Å and containing the infrared calcium triplet – for the analysis in this paper.

The strong unambiguous RGB signal, and the availability of the colour–magnitude, proper motion, and spatial information allowed easy and efficient target selection. Fig. 4 gives the DECam colour–magnitude diagram of the targets selected for the spectroscopic follow-up. Note that the original selection was performed using *Gaia*'s BP and RP band-passes, which is why the selection deviates substantially from the isochrone colours at fainter magnitudes. On top of the CMD-based selection, we also required the targets to have proper motions within 1.5 mas yr^{-1} of $(\mu_\alpha \cos\delta, \mu_\delta) = (-0.04, -0.04)$ mas yr^{-1}. The targets were selected to occupy the whole of the 2 deg field of view of the 2dF + AAOmega spectrograph. We observed a total of 349 candidate stars in Ant 2.

The data reduction was performed using the latest version of the 2*dfdr* package (v6.46),[2] including the following procedures: bias subtraction, 2D scattered light subtraction, flat-fielding, Gaussian-weighted spectral extraction, wavelength calibration, sky subtraction, and spectrum combination.

To model the observed spectra and obtain chemical abundances and radial velocities we use a direct pixel-fitting approach by interpolated spectral templates (see e.g. Koleva et al. 2009; Koposov et al. 2011; Walker, Olszewski & Mateo 2015). We use the PHOENIX v2.0 spectral library (Husser et al. 2013) that spans a large range of metallicities (from [Fe/H] = −4 to [Fe/H] = 1, [α/*Fe*] between −0.2 and 1.2) and stellar atmospheric parameters. For parameter values that fall between templates, we combine the radial basis function interpolation, which is used to create a grid with a step size finer than that in the original PHOENIX grid, with a linear N-d interpolation based on the Delaunay triangulation (Hormann 2014) (at the last stage). At each spectral-fitting step, the polynomial continuum correction transforming the template into observed data is determined. As the original template grid has $\log g$, $T_{\rm eff}$, [Fe/H], and α parameters, we sample those together with the radial velocity using the emcee (Foreman-Mackey et al. 2013) ensemble sampler, while assuming uniform priors over all parameters. The resulting chains for each parameter of interest are then used to

[2] https://www.aao.gov.au/science/software/2dfdr

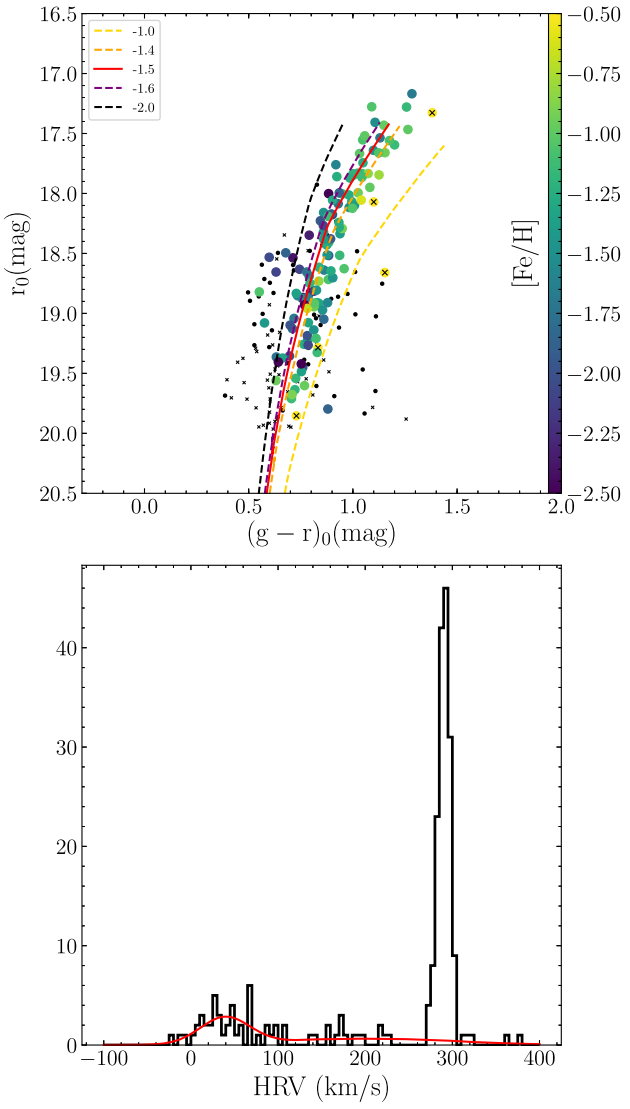

Figure 4. *Top:* CMD of the stars with spectroscopic measurements within the DECam data footprint. Ant 2 stars with accurate velocity measurements are colour-coded according to their spectroscopic metallicity. Small black dots are stars with velocities inconsistent with Ant 2 membership and small black crosses are stars without good velocity measurements. The red line corresponds to the best-fitting isochrone from the photometric modelling, while the dashed lines show isochrones with the same age, but different metallicity values. Reassuringly, there is a good correlation between the spectroscopic metallicity of each star and the general [$(g-r)_0$ colour] trend marked by the different isochrones. The large spread in the spectroscopic metallicity of Ant 2 stars appears to be consistent with the large width of the RGB. *Bottom:* Distribution of heliocentric radial velocities of the targeted stars. Only stars with accurate velocity measurements are shown (uncertainties less than 10 km s^{-1}, residual kurtosis and skewness less than 1). The red curve shows the best-fitting foreground model, consisting of two Gaussian distributions.

measure various statistics, such as posterior percentiles and standard deviations, as well as the measures of non-Gaussianity, such as kurtosis and skewness (as motivated by Walker et al. 2015). The average signal-to-noise (per pixel) of the spectra is 5.8, and for the spectra with S/N>3 the median uncertainties were 2.67 km s^{-1}, 0.7 dex, 325 K, and 0.35 dex for the RV, log g, $T_{\rm eff}$, and [Fe/H], respectively. Most radial velocity uncertainties are significantly larger than the systematic floor of 0.5 km s^{-1} of the 1700D setup on AAOmega (Koposov, private communication). Table 2 records all the relevant information for the spectroscopic measurements reported here.

For the most part, the analysis of the stellar kinematics in the paper utilizes the subset of stars with 1σ uncertainties in the radial velocity less than 10 km s^{-1} and residual kurtosis and skewness less than 1 in absolute value in order to ensure that the posterior is close enough to a Gaussian. The number of these stars is 221. The velocity distribution of these stars is shown in Fig. 4. The distribution reveals a strikingly prominent peak at ∼290 km s^{-1} containing 159 of the 221 stars in the sample – undoubtedly Ant 2's velocity signature – as well as a broad (and weak) contribution from the MW halo and MW disc. The association of the velocity peak with Ant 2 is particularly clear in Fig. 5, where we show the radial velocities of the observed stars as a function of their proper motion and spectroscopic metallicity. The stars in the RV peak have metallicities significantly lower than the field stars and are concentrated around the proper motion value of $(\mu_\alpha \cos\delta, \mu_\delta) \approx (0, 0)$. In the next section, we model the observed distribution to measure the kinematic properties of the newly discovered dwarf.

3.1 Kinematic modelling

To describe the kinematics of the system we construct a generative model of the proper motions and radial velocities. The right two panels of Fig. 5 show the data used for the model. We highlight that both the proper motions and radial velocities are highly informative for identification of members of Antlia 2, however the proper motion errors are noticeably larger. For the foreground contaminants, our model assumes a two-component Gaussian mixture distribution in radial velocity and a uniform distribution over proper motions within our selection box. The radial velocity distribution of the Antlia 2 members is modelled by a Gaussian, while the proper motions are assumed to have no intrinsic scatter and therefore are described by a delta function as specified below:

$$\begin{aligned}\mathcal{P}(\boldsymbol{\mu}, V|\alpha, \delta) = (1-f_o)(f_{b,1}N(V|V_{b,1}, \sigma_{b,1}) \\ +(1-f_{b,1})N(V|V_{b,2}, \sigma_{b,2}))U(\boldsymbol{\mu}) \\ +f_o N(V|V_o, \sigma_o))\delta(\boldsymbol{\mu}-\boldsymbol{\mu}_o) \qquad (2)\end{aligned}$$

where f_o is the fraction of stars belonging to Ant 2 and $f_{b,1}$ is the fraction of the foreground stars belonging to a first Gaussian component, V_o and σ_o are the systemic velocity and the velocity dispersion of Ant 2, and $V_{b,1}$, $V_{b,2}$, $\sigma_{b,1}$, $\sigma_{b,2}$ are the means and standard deviations of the Gaussian distribution of the foreground. $U(\boldsymbol{\mu})$ is the bivariate uniform distribution within the proper motion selection region. The Gaussian uncertainties on both proper motions and radial velocities for each star are easily taken into account in this model by convolving the distribution with the appropriate Gaussian. The only additional assumption we make to take into account the uncertainties is that the contaminants are approximately uniformly distributed over a much larger area than the proper motion selection area. We note also that the probability distribution in equation (2) is conditioned on Right Ascension and Declination, as some of the variants of the model described below consider the dependence of the systemic velocity and the proper motion V_o and μ_o on the star's position.

Because Ant 2 is exceptionally extended on the sky, we consider a situation where the systemic velocity of the object can spatially vary across the object. Such velocity field evolution could be

Table 2. Results from the spectroscopic modelling.

id	RA (deg)	Dec. (deg)	rv_h (km s^{-1})	[Fe/H] (dex)	log g (dex)	T_{eff} (K)
Antlia2_001	144.41	−36.7678	290.2 ± 0.7	− 1.33 ± 0.17	1.19 ± 0.29	4955 ± 83
Antlia2_002	144.0322	−36.7156	294.0 ± 0.9	− 1.12 ± 0.11	4.39 ± 0.23	4668 ± 118
Antlia2_003	144.5626	−36.8088	275.1 ± 9.8	− 2.39 ± 0.54	4.02 ± 1.37	4943 ± 281
Antlia2_004	144.2164	−36.7546	289.3 ± 3.4	− 1.34 ± 0.38	3.22 ± 0.88	4958 ± 221
Antlia2_005	144.6405	−36.9363	284.2 ± 3.9	− 1.44 ± 0.38	3.75 ± 0.86	4860 ± 221
Antlia2_006	143.8835	−36.7709	292.9 ± 0.8	− 1.1 ± 0.12	1.3 ± 0.26	5075 ± 57
Antlia2_007	144.2962	−36.8591	278.3 ± 4.1	− 1.62 ± 0.35	2.7 ± 0.93	4884 ± 223
Antlia2_008	144.8393	−37.0967	8.6 ± 3.1	0.23 ± 0.32	5.2 ± 0.64	4629 ± 185
Antlia2_009	144.738	−37.0794	20.4 ± 3.4	− 0.48 ± 0.33	4.98 ± 0.68	4698 ± 331
Antlia2_010	144.3932	−36.9902	288.5 ± 1.4	− 1.23 ± 0.17	3.91 ± 0.27	4428 ± 125
Antlia2_011	144.0758	−36.8442	290.2 ± 1.9	− 1.29 ± 0.26	3.88 ± 0.52	4711 ± 260
Antlia2_012	144.2665	−36.9975	48.4 ± 3.9	− 0.22 ± 0.34	5.28 ± 0.54	5008 ± 220
Antlia2_013	144.6282	−37.1997	293.0 ± 2.5	− 1.2 ± 0.29	3.96 ± 0.7	4746 ± 201
Antlia2_014	144.0369	−36.9445	288.0 ± 1.7	− 1.16 ± 0.25	3.63 ± 0.66	4960 ± 218
Antlia2_015	144.0136	−36.8662	287.8 ± 5.4	− 1.31 ± 0.28	4.81 ± 0.63	5136 ± 264
Antlia2_016	144.3143	−37.0689	292.8 ± 1.2	− 0.94 ± 0.13	3.8 ± 0.23	4287 ± 83
Antlia2_017	144.5795	−37.2524	289.2 ± 2.5	− 1.16 ± 0.26	2.95 ± 0.74	4926 ± 196
Antlia2_018	144.4075	−37.1573	293.1 ± 1.3	− 1.0 ± 0.12	2.02 ± 0.61	5115 ± 138
Antlia2_019	144.256	−37.0773	291.0 ± 1.8	− 1.26 ± 0.21	3.84 ± 0.52	4701 ± 202
Antlia2_020	144.2549	−37.1559	272.2 ± 6.8	− 1.24 ± 0.54	4.58 ± 1.06	4865 ± 340
Antlia2_021	144.323	−37.1384	291.8 ± 1.8	− 1.25 ± 0.25	2.42 ± 0.8	4957 ± 149
Antlia2_022	144.5144	−37.3139	85.6 ± 2.8	− 0.97 ± 0.28	4.16 ± 0.61	5124 ± 231
Antlia2_023	144.6594	−37.4486	294.1 ± 2.4	− 1.07 ± 0.23	4.29 ± 0.5	4723 ± 198
Antlia2_024	144.185	−37.1481	283.7 ± 3.2	− 1.4 ± 0.26	4.54 ± 0.6	4688 ± 249
Antlia2_025	144.3197	−37.2287	289.4 ± 0.9	− 0.84 ± 0.12	4.28 ± 0.26	4827 ± 136
Antlia2_026	144.013	−36.9676	300.2 ± 0.6	− 0.79 ± 0.09	3.9 ± 0.14	4408 ± 73
Antlia2_027	144.2995	−37.2668	280.1 ± 3.2	− 1.47 ± 0.41	2.55 ± 1.37	4974 ± 239
Antlia2_028	144.0498	−37.0218	273.0 ± 6.5	− 0.37 ± 0.45	5.19 ± 0.9	5046 ± 320
Antlia2_029	144.1539	−37.1801	314.7 ± 0.8	− 0.14 ± 0.17	2.81 ± 0.37	4034 ± 103
Antlia2_030	144.4285	−37.4949	297.3 ± 2.6	− 1.24 ± 0.29	2.62 ± 0.81	5024 ± 196
Antlia2_031	144.2236	−37.302	281.7 ± 6.3	− 2.02 ± 0.64	3.53 ± 1.37	4799 ± 385
Antlia2_032	144.3628	−37.4769	285.5 ± 4.1	− 1.75 ± 0.44	2.63 ± 0.96	4707 ± 247
Antlia2_033	144.0026	−37.0409	292.1 ± 0.8	− 1.0 ± 0.09	3.65 ± 0.59	4355 ± 246
Antlia2_034	144.3108	−37.4548	294.8 ± 0.9	− 1.67 ± 0.18	1.36 ± 0.4	4937 ± 102
Antlia2_035	144.0247	−37.1193	85.8 ± 1.5	− 1.58 ± 0.5	5.93 ± 0.32	3834 ± 216
Antlia2_036	144.1418	−37.3015	296.0 ± 0.7	− 1.14 ± 0.1	3.96 ± 0.14	4399 ± 61
Antlia2_037	144.081	−37.1197	288.4 ± 2.0	− 0.91 ± 0.25	3.51 ± 0.64	4856 ± 202
Antlia2_038	144.0853	−37.259	295.3 ± 2.8	− 1.57 ± 0.31	3.45 ± 0.94	4748 ± 239
Antlia2_039	144.0885	−37.1639	288.3 ± 5.5	− 2.18 ± 0.49	2.91 ± 1.17	4828 ± 323
Antlia2_040	144.189	−37.4559	292.4 ± 1.2	− 1.39 ± 0.19	2.96 ± 0.55	4798 ± 164
Antlia2_041	144.1202	−37.3303	296.2 ± 3.5	− 1.44 ± 0.6	2.81 ± 1.14	4858 ± 408
Antlia2_042	143.9548	−36.9605	284.2 ± 6.5	− 1.16 ± 0.38	4.38 ± 0.85	4985 ± 312
Antlia2_043	144.1308	−37.668	292.0 ± 2.6	− 1.32 ± 0.22	4.32 ± 0.5	4589 ± 226
Antlia2_044	143.8916	−37.1604	295.6 ± 2.3	− 1.19 ± 0.42	2.09 ± 1.01	4889 ± 201
Antlia2_045	143.8625	−37.1026	293.8 ± 1.3	− 1.52 ± 0.2	3.67 ± 0.53	4654 ± 150
Antlia2_046	143.9378	−37.3905	286.4 ± 4.2	− 1.42 ± 0.42	3.64 ± 0.93	5240 ± 285
Antlia2_047	143.8282	−37.132	218.4 ± 4.6	− 1.3 ± 0.39	2.93 ± 1.31	5144 ± 296
Antlia2_048	144.0119	−37.7311	291.2 ± 2.3	− 1.88 ± 0.29	2.82 ± 0.55	4634 ± 245
Antlia2_049	143.9227	−37.4917	293.3 ± 3.1	− 1.93 ± 0.72	3.83 ± 1.0	5108 ± 537
Antlia2_050	143.8137	−37.1636	174.1 ± 3.2	− 1.15 ± 0.46	2.69 ± 1.73	4682 ± 294
Antlia2_051	143.7889	−37.101	300.4 ± 0.9	− 0.99 ± 0.13	2.22 ± 0.36	5119 ± 72
Antlia2_052	143.7875	−37.2203	290.4 ± 0.9	− 1.25 ± 0.17	1.89 ± 0.37	5069 ± 73
Antlia2_053	143.7774	−37.5246	303.9 ± 1.0	− 1.48 ± 0.19	2.18 ± 0.57	4739 ± 148
Antlia2_054	143.7444	−37.6849	273.4 ± 6.7	− 2.55 ± 0.57	3.84 ± 1.56	4727 ± 254
Antlia2_055	143.7364	−37.5761	282.0 ± 4.8	− 3.31 ± 0.67	2.83 ± 1.66	4458 ± 283
Antlia2_056	143.7462	−37.1284	292.3 ± 0.6	− 1.06 ± 0.14	1.9 ± 0.33	5036 ± 68
Antlia2_057	143.6452	−37.6683	57.8 ± 7.2	− 1.03 ± 0.63	6.07 ± 1.09	4881 ± 372
Antlia2_058	143.5564	−37.6037	296.8 ± 2.0	− 1.27 ± 0.24	3.42 ± 0.62	4826 ± 200
Antlia2_059	143.6555	−37.0654	280.9 ± 2.0	− 1.08 ± 0.28	3.63 ± 0.75	4993 ± 205
Antlia2_060	143.5162	−37.3626	287.6 ± 1.5	− 1.26 ± 0.25	2.57 ± 0.45	5137 ± 143
Antlia2_061	143.865	−36.8063	296.1 ± 3.2	− 1.68 ± 0.42	1.68 ± 0.96	5025 ± 278
Antlia2_062	143.545	−37.2742	293.4 ± 0.5	− 1.71 ± 0.04	1.02 ± 0.08	4796 ± 14

Table 2 – *continued*

id	RA (deg)	Dec. (deg)	rv_h (km s^{-1})	[Fe/H] (dex)	log g (dex)	T_{eff} (K)
Antlia2_063	143.4109	−37.5214	51.7 ± 4.6	− 0.92 ± 0.55	5.82 ± 1.13	4574 ± 344
Antlia2_064	143.4977	−37.3211	47.7 ± 3.0	− 1.06 ± 0.36	4.88 ± 0.67	4908 ± 203
Antlia2_065	143.3955	−37.4922	− 24.5 ± 3.9	− 0.24 ± 0.35	5.22 ± 0.65	4611 ± 323
Antlia2_066	143.3652	−37.4772	294.4 ± 4.9	− 2.0 ± 0.54	2.55 ± 1.25	4821 ± 331
Antlia2_067	143.4774	−37.1417	298.4 ± 0.2	− 0.29 ± 0.03	2.49 ± 0.11	3995 ± 17
Antlia2_068	143.5907	−37.0158	296.2 ± 7.2	− 1.87 ± 0.72	4.42 ± 1.22	4856 ± 416
Antlia2_069	143.523	−37.2347	300.2 ± 4.7	− 1.36 ± 0.56	3.73 ± 1.12	4660 ± 280
Antlia2_070	143.5213	−37.1668	290.7 ± 2.7	− 1.75 ± 0.33	3.43 ± 0.98	4741 ± 242
Antlia2_071	143.0966	−37.5431	289.2 ± 2.2	− 1.48 ± 0.27	2.52 ± 0.73	4824 ± 171
Antlia2_072	143.7441	−36.9139	29.5 ± 3.7	− 1.05 ± 0.41	3.71 ± 1.07	4971 ± 328
Antlia2_073	143.455	−37.0521	287.6 ± 2.3	− 2.0 ± 0.29	1.71 ± 0.84	4928 ± 206
Antlia2_074	143.5503	−36.9872	278.5 ± 2.8	− 1.32 ± 0.31	3.36 ± 0.81	5178 ± 230
Antlia2_075	143.5367	−37.0773	298.8 ± 3.8	− 1.81 ± 0.55	1.76 ± 0.96	4852 ± 285
Antlia2_076	143.018	−37.4241	294.7 ± 5.7	− 2.44 ± 0.64	4.15 ± 1.48	4672 ± 428
Antlia2_077	143.0292	−37.31	109.9 ± 3.6	− 0.83 ± 0.38	5.12 ± 0.84	4622 ± 329
Antlia2_078	142.894	−37.3983	301.4 ± 3.0	− 1.98 ± 0.49	3.22 ± 0.72	4859 ± 253
Antlia2_079	143.8168	−36.7829	292.7 ± 2.2	− 1.36 ± 0.38	2.64 ± 0.93	4793 ± 212
Antlia2_080	142.9567	−37.3225	285.2 ± 0.9	− 2.74 ± 0.15	0.67 ± 0.28	4492 ± 73
Antlia2_081	143.1255	−37.2181	138.6 ± 3.0	− 1.67 ± 0.5	3.25 ± 0.88	4967 ± 225
Antlia2_082	142.7703	−37.3498	172.1 ± 2.9	− 1.07 ± 0.43	3.59 ± 0.79	5080 ± 208
Antlia2_083	143.399	−36.9386	281.4 ± 3.8	− 2.45 ± 0.5	2.54 ± 1.17	4601 ± 259
Antlia2_084	143.6257	−36.8654	293.3 ± 4.1	− 2.05 ± 0.47	4.19 ± 1.07	5064 ± 385
Antlia2_085	143.4277	−36.8772	295.0 ± 2.5	− 0.99 ± 0.45	2.39 ± 0.89	4934 ± 241
Antlia2_086	143.6338	−36.9415	285.3 ± 4.9	− 1.19 ± 0.53	2.04 ± 1.43	5377 ± 317
Antlia2_087	143.0142	−37.1148	11.3 ± 2.5	0.03 ± 0.43	5.72 ± 0.49	4549 ± 275
Antlia2_088	142.7531	−37.2389	44.2 ± 4.7	− 1.97 ± 0.35	5.85 ± 0.33	4510 ± 277
Antlia2_089	143.6367	−36.7939	286.1 ± 6.3	− 1.46 ± 0.57	4.45 ± 1.07	4908 ± 321
Antlia2_090	143.1911	−36.9777	298.6 ± 0.9	− 1.42 ± 0.22	2.16 ± 0.66	4914 ± 121
Antlia2_091	143.7745	−36.8622	292.6 ± 1.7	− 1.21 ± 0.19	2.67 ± 0.53	5148 ± 143
Antlia2_092	143.5555	−36.7636	282.0 ± 2.7	− 1.58 ± 0.39	2.69 ± 0.83	4616 ± 241
Antlia2_093	143.5135	−36.8184	298.7 ± 1.2	− 2.04 ± 0.24	2.28 ± 0.51	4754 ± 133
Antlia2_094	143.3822	−36.8418	289.5 ± 0.5	− 0.96 ± 0.08	3.69 ± 0.12	4314 ± 61
Antlia2_095	143.0311	−36.8743	289.2 ± 1.2	− 1.25 ± 0.18	3.46 ± 0.41	4795 ± 189
Antlia2_096	143.248	−36.8216	287.8 ± 1.1	− 2.32 ± 0.22	2.13 ± 0.43	4677 ± 139
Antlia2_097	143.381	−36.6321	301.7 ± 3.7	− 1.73 ± 0.41	3.12 ± 1.09	5052 ± 305
Antlia2_098	143.0082	−36.8738	195.3 ± 3.3	− 1.59 ± 0.4	3.26 ± 1.02	4877 ± 211
Antlia2_099	143.044	−36.8536	294.7 ± 1.2	− 2.28 ± 0.21	2.06 ± 0.37	4789 ± 154
Antlia2_100	143.2149	−36.805	289.8 ± 1.9	− 1.28 ± 0.25	2.69 ± 0.7	4827 ± 190
Antlia2_101	143.4385	−36.641	296.1 ± 1.0	− 1.07 ± 0.19	2.07 ± 0.39	5042 ± 98
Antlia2_102	142.7956	−36.8848	31.0 ± 3.6	− 1.78 ± 0.4	4.35 ± 0.97	4470 ± 300
Antlia2_103	142.984	−36.8579	3.9 ± 1.3	− 0.39 ± 0.15	5.35 ± 0.34	5123 ± 196
Antlia2_104	143.0315	−36.7567	299.1 ± 3.5	− 2.05 ± 0.51	0.01 ± 1.14	4899 ± 337
Antlia2_105	143.4262	−36.7238	287.9 ± 1.7	− 1.0 ± 0.23	2.08 ± 0.66	5035 ± 148
Antlia2_106	143.485	−36.6694	29.4 ± 3.3	0.04 ± 0.3	5.58 ± 1.01	4834 ± 313
Antlia2_107	143.567	−36.6938	293.5 ± 3.8	− 1.35 ± 0.76	3.04 ± 1.07	5391 ± 461
Antlia2_108	142.54	−36.6496	69.9 ± 6.3	− 1.08 ± 0.58	5.89 ± 0.64	3966 ± 619
Antlia2_109	142.48	−36.6232	315.4 ± 5.9	− 0.43 ± 0.54	5.47 ± 0.67	5021 ± 199
Antlia2_110	142.5243	−36.6079	286.2 ± 9.2	− 1.88 ± 0.8	2.88 ± 1.41	4869 ± 239
Antlia2_111	143.0022	−36.6454	294.2 ± 3.8	− 2.09 ± 0.34	3.28 ± 0.71	4860 ± 228
Antlia2_112	143.1721	−36.6686	97.5 ± 4.2	− 0.45 ± 0.43	5.32 ± 0.86	4399 ± 315
Antlia2_113	142.8796	−36.5792	291.3 ± 2.0	− 1.53 ± 0.29	2.66 ± 0.61	4483 ± 199
Antlia2_114	142.715	−36.5071	− 13.1 ± 4.4	− 0.71 ± 0.47	2.34 ± 1.91	4645 ± 372
Antlia2_115	143.0283	−36.5595	300.4 ± 1.2	− 1.52 ± 0.21	2.42 ± 1.01	4731 ± 151
Antlia2_116	143.3247	−36.6292	298.7 ± 1.2	− 1.47 ± 0.21	3.47 ± 0.51	4887 ± 156
Antlia2_117	143.0218	−36.5246	27.8 ± 3.2	− 0.18 ± 0.32	5.46 ± 0.66	4564 ± 302
Antlia2_118	142.9719	−36.4776	299.6 ± 0.4	0.33 ± 0.21	1.14 ± 0.38	3465 ± 204
Antlia2_119	143.2491	−36.5633	293.0 ± 0.5	− 0.97 ± 0.09	3.49 ± 0.14	4305 ± 71
Antlia2_120	143.48	−36.5207	170.4 ± 3.3	− 1.27 ± 0.4	5.06 ± 0.73	5408 ± 283
Antlia2_121	143.1997	−36.5209	45.0 ± 2.9	0.25 ± 0.3	4.63 ± 0.94	4894 ± 319
Antlia2_122	143.6304	−36.5916	292.5 ± 1.0	− 1.21 ± 0.17	2.33 ± 0.68	4830 ± 223
Antlia2_123	143.4508	−36.526	297.5 ± 3.7	− 1.83 ± 0.52	4.71 ± 0.9	4947 ± 314
Antlia2_124	143.4412	−36.7202	288.6 ± 4.8	− 0.54 ± 0.49	3.09 ± 1.23	5324 ± 337

Table 2 – *continued*

id	RA (deg)	Dec. (deg)	rv_h (km s^{-1})	[Fe/H] (dex)	log g (dex)	T_{eff} (K)
Antlia2_125	142.679	−36.2331	289.1 ± 1.4	−1.45 ± 0.31	2.31 ± 0.7	4687 ± 187
Antlia2_126	142.9998	−36.3547	18.2 ± 4.9	−0.45 ± 0.69	4.44 ± 1.4	4955 ± 447
Antlia2_127	143.1023	−36.3311	292.8 ± 3.5	−1.62 ± 0.36	2.96 ± 0.92	4677 ± 274
Antlia2_128	143.3845	−36.536	281.1 ± 1.8	−1.51 ± 0.21	1.61 ± 0.57	5014 ± 178
Antlia2_129	142.8157	−36.2154	288.6 ± 5.8	−1.18 ± 0.63	0.98 ± 1.21	4827 ± 310
Antlia2_130	143.5783	−36.6125	287.5 ± 0.9	−1.24 ± 0.11	3.87 ± 0.19	4392 ± 85
Antlia2_131	143.0325	−36.2573	280.0 ± 1.7	−1.05 ± 0.26	3.39 ± 0.59	4978 ± 254
Antlia2_132	143.6435	−36.5501	289.6 ± 1.3	−1.96 ± 0.23	1.44 ± 0.44	4766 ± 113
Antlia2_133	143.6242	−36.4029	283.3 ± 2.7	−2.17 ± 0.39	2.52 ± 0.74	4633 ± 234
Antlia2_134	143.1325	−36.2867	77.2 ± 3.7	0.1 ± 0.27	5.38 ± 0.52	5031 ± 272
Antlia2_135	143.5472	−36.3937	295.0 ± 3.9	−1.71 ± 0.39	3.47 ± 0.97	4684 ± 270
Antlia2_136	143.029	−36.1825	430.5 ± 7.3	−1.78 ± 0.5	5.02 ± 0.9	5020 ± 322
Antlia2_137	142.9986	−36.1471	194.0 ± 5.5	−1.91 ± 0.55	2.76 ± 1.77	5326 ± 359
Antlia2_138	143.6291	−36.4992	289.2 ± 3.4	−2.03 ± 0.47	4.13 ± 0.94	4535 ± 312
Antlia2_139	143.5753	−36.4902	295.3 ± 1.2	−1.93 ± 0.23	1.09 ± 0.44	4803 ± 123
Antlia2_140	143.6256	−36.5625	295.7 ± 2.7	−0.72 ± 0.36	3.56 ± 1.19	5032 ± 260
Antlia2_141	143.0544	−36.0141	44.3 ± 3.6	−0.48 ± 0.25	4.88 ± 0.7	4651 ± 220
Antlia2_142	143.1813	−36.1775	280.8 ± 3.6	−1.14 ± 0.39	2.83 ± 1.59	4747 ± 282
Antlia2_143	142.9533	−35.9304	290.0 ± 7.1	−2.72 ± 0.6	5.48 ± 1.54	3997 ± 263
Antlia2_144	143.2108	−36.1181	29.9 ± 3.0	0.11 ± 0.24	5.28 ± 0.58	4473 ± 219
Antlia2_145	143.1267	−35.9899	288.9 ± 1.3	−1.6 ± 0.26	2.23 ± 0.64	4791 ± 135
Antlia2_146	143.0852	−35.9434	34.0 ± 4.4	−1.79 ± 0.6	5.74 ± 0.42	4041 ± 294
Antlia2_147	143.2008	−36.1824	65.4 ± 10.0	−1.88 ± 0.72	5.01 ± 1.17	4502 ± 420
Antlia2_148	143.1406	−35.979	9.7 ± 3.2	−0.91 ± 0.34	5.16 ± 0.81	4389 ± 276
Antlia2_149	143.278	−36.148	290.5 ± 3.2	−1.61 ± 0.41	2.66 ± 0.84	5113 ± 259
Antlia2_150	143.3024	−36.236	295.0 ± 6.6	−2.25 ± 0.66	2.05 ± 1.53	4393 ± 344
Antlia2_151	143.2906	−35.9939	13.2 ± 4.0	−0.77 ± 0.58	5.55 ± 1.01	4741 ± 272
Antlia2_152	143.2522	−35.967	159.2 ± 1.5	−0.86 ± 0.24	4.74 ± 0.49	5128 ± 234
Antlia2_153	143.487	−36.2642	296.8 ± 2.6	−2.14 ± 0.35	2.5 ± 0.68	4853 ± 244
Antlia2_154	143.6713	−36.3644	140.1 ± 3.2	−2.11 ± 0.3	3.17 ± 0.94	4955 ± 207
Antlia2_155	143.2321	−35.8358	286.6 ± 4.1	−2.1 ± 0.53	4.68 ± 1.06	5106 ± 246
Antlia2_156	143.3072	−35.9445	158.8 ± 4.3	−0.85 ± 0.65	3.85 ± 1.33	5423 ± 363
Antlia2_157	143.442	−36.0378	290.9 ± 2.4	−1.36 ± 0.31	2.83 ± 0.75	4850 ± 172
Antlia2_158	143.6224	−36.2775	301.7 ± 0.7	−1.25 ± 0.19	1.36 ± 0.34	4971 ± 95
Antlia2_159	143.4061	−35.957	296.2 ± 2.7	−2.6 ± 0.36	1.69 ± 0.74	4620 ± 114
Antlia2_160	143.5705	−36.0955	288.1 ± 2.3	−1.72 ± 0.31	3.23 ± 0.72	4872 ± 207
Antlia2_161	143.5017	−35.8606	274.8 ± 1.9	−1.87 ± 0.29	1.61 ± 0.78	4633 ± 173
Antlia2_162	143.5503	−35.9301	284.7 ± 3.1	−2.04 ± 0.42	3.4 ± 0.84	5120 ± 171
Antlia2_163	143.606	−36.0869	288.3 ± 6.0	−2.51 ± 0.94	4.93 ± 1.12	4317 ± 405
Antlia2_164	143.5992	−35.9915	287.0 ± 0.9	−1.22 ± 0.11	3.83 ± 0.73	4447 ± 196
Antlia2_165	143.6506	−36.2201	294.3 ± 1.4	−1.39 ± 0.22	2.17 ± 0.6	5036 ± 139
Antlia2_166	143.7377	−36.0909	185.4 ± 1.6	−0.26 ± 0.21	3.56 ± 0.62	5084 ± 168
Antlia2_167	143.6639	−36.2787	287.2 ± 0.6	−0.99 ± 0.16	1.73 ± 0.72	4860 ± 122
Antlia2_168	143.6661	−35.9863	34.9 ± 4.6	−0.81 ± 0.51	5.03 ± 2.29	4350 ± 276
Antlia2_169	143.6968	−35.7993	287.3 ± 1.9	−0.94 ± 0.24	2.8 ± 0.6	4891 ± 171
Antlia2_170	143.7152	−35.8785	285.4 ± 4.9	−2.49 ± 0.6	2.45 ± 1.44	4596 ± 339
Antlia2_171	143.762	−35.7853	284.8 ± 1.7	−1.04 ± 0.21	2.07 ± 0.58	4882 ± 155
Antlia2_172	143.7126	−36.4737	294.6 ± 0.9	−1.13 ± 0.16	1.79 ± 0.33	5012 ± 98
Antlia2_173	143.7959	−36.0037	288.7 ± 0.7	−0.98 ± 0.11	1.81 ± 0.26	5084 ± 66
Antlia2_174	143.7845	−36.1298	287.2 ± 1.2	−1.07 ± 0.17	3.34 ± 0.65	5000 ± 161
Antlia2_175	143.7935	−36.2443	27.3 ± 2.4	−0.29 ± 0.24	5.08 ± 0.47	4873 ± 180
Antlia2_176	143.6763	−36.3421	223.7 ± 2.3	−1.03 ± 0.32	2.69 ± 0.89	5169 ± 195
Antlia2_177	143.8092	−36.2361	281.9 ± 3.3	−1.34 ± 0.36	3.83 ± 0.85	5254 ± 262
Antlia2_178	143.8774	−35.9471	217.0 ± 3.9	−1.69 ± 0.44	3.02 ± 0.83	5170 ± 226
Antlia2_179	143.9661	−35.7902	295.7 ± 6.2	−1.42 ± 0.48	3.94 ± 1.15	5203 ± 288
Antlia2_180	143.6692	−36.3141	91.8 ± 2.4	0.21 ± 0.19	4.77 ± 0.52	4967 ± 189
Antlia2_181	143.9801	−35.7549	284.2 ± 3.2	−1.28 ± 0.58	1.51 ± 1.48	4817 ± 356
Antlia2_182	143.8865	−36.0804	280.7 ± 2.4	−1.87 ± 0.3	1.47 ± 1.07	4941 ± 147
Antlia2_183	143.834	−36.2541	360.4 ± 3.8	−0.26 ± 0.4	4.84 ± 0.63	5785 ± 335
Antlia2_184	143.8395	−36.3661	295.2 ± 1.9	−1.45 ± 0.27	1.8 ± 0.56	4843 ± 167
Antlia2_185	143.6866	−36.5661	281.9 ± 4.2	−1.41 ± 0.35	4.03 ± 0.88	4867 ± 286
Antlia2_186	143.942	−36.2156	66.4 ± 2.8	0.1 ± 0.21	5.65 ± 0.38	5037 ± 211

Table 2 – *continued*

id	RA (deg)	Dec. (deg)	rv_h (km s^{-1})	[Fe/H] (dex)	log g (dex)	T_{eff} (K)
Antlia2_187	143.6558	−36.5768	297.8 ± 0.6	− 1.0 ± 0.09	1.7 ± 0.26	5098 ± 50
Antlia2_188	144.1966	−35.7793	276.5 ± 5.3	− 1.98 ± 0.54	4.07 ± 1.48	4682 ± 266
Antlia2_189	144.2014	−35.8191	65.2 ± 6.6	− 0.86 ± 0.38	5.67 ± 0.49	4543 ± 276
Antlia2_190	144.0545	−36.2081	59.3 ± 5.4	0.04 ± 0.37	5.55 ± 0.7	4940 ± 337
Antlia2_191	144.1003	−36.0622	378.8 ± 3.6	− 1.75 ± 0.52	2.58 ± 0.85	5118 ± 212
Antlia2_192	144.0123	−36.2622	295.1 ± 1.5	− 1.11 ± 0.17	2.89 ± 0.46	4998 ± 136
Antlia2_193	144.254	−35.8732	169.3 ± 3.4	− 0.63 ± 0.32	4.43 ± 0.98	5160 ± 215
Antlia2_194	144.1068	−36.1388	288.5 ± 1.2	− 1.85 ± 0.16	0.97 ± 0.4	4844 ± 100
Antlia2_195	144.239	−36.0789	38.8 ± 1.0	0.17 ± 0.12	4.74 ± 0.28	4553 ± 98
Antlia2_196	144.2908	−36.0961	95.7 ± 3.0	− 0.14 ± 0.23	5.06 ± 0.55	4501 ± 218
Antlia2_197	144.3403	−35.9994	107.3 ± 2.4	− 0.29 ± 0.28	4.45 ± 0.51	4707 ± 235
Antlia2_198	144.307	−36.1008	289.2 ± 1.2	− 2.06 ± 0.21	1.53 ± 0.45	4699 ± 133
Antlia2_199	144.1083	−36.2986	226.1 ± 0.7	− 0.68 ± 0.1	4.18 ± 0.18	4764 ± 103
Antlia2_200	144.0819	−36.3793	275.6 ± 4.6	− 0.95 ± 0.39	3.4 ± 1.0	5128 ± 241
Antlia2_201	144.3462	−36.2044	281.7 ± 2.9	− 1.46 ± 0.3	4.38 ± 0.77	4971 ± 234
Antlia2_202	144.5744	−36.0101	19.0 ± 4.5	− 0.93 ± 0.85	5.03 ± 0.87	4963 ± 268
Antlia2_203	144.0653	−36.4794	295.3 ± 0.4	− 1.16 ± 0.12	1.26 ± 0.24	4940 ± 46
Antlia2_204	144.2034	−36.365	297.9 ± 2.2	− 1.33 ± 0.3	3.19 ± 0.85	4756 ± 234
Antlia2_205	143.9453	−36.7579	320.6 ± 4.6	− 1.05 ± 0.45	3.34 ± 1.46	5112 ± 243
Antlia2_206	144.3255	−36.3558	290.4 ± 0.5	− 1.07 ± 0.06	1.12 ± 0.11	4985 ± 33
Antlia2_207	144.1495	−36.6055	297.7 ± 6.3	− 0.96 ± 0.52	4.59 ± 1.04	4834 ± 348
Antlia2_208	144.2508	−36.4576	65.5 ± 2.2	− 0.24 ± 0.19	5.47 ± 0.43	4750 ± 149
Antlia2_209	144.2995	−36.4365	279.2 ± 0.6	− 1.05 ± 0.09	4.01 ± 0.14	4397 ± 76
Antlia2_210	144.2863	−36.5128	287.3 ± 0.9	− 0.61 ± 0.12	3.77 ± 0.23	4679 ± 119
Antlia2_211	144.4146	−36.4728	46.9 ± 1.3	0.15 ± 0.12	5.49 ± 0.28	4890 ± 106
Antlia2_212	144.267	−36.5383	293.0 ± 1.2	− 1.27 ± 0.17	2.95 ± 0.64	4904 ± 114
Antlia2_213	144.2461	−36.5839	65.3 ± 6.3	− 0.28 ± 0.48	4.52 ± 1.08	4193 ± 307
Antlia2_214	144.3061	−36.5282	299.8 ± 5.0	− 1.49 ± 0.35	3.23 ± 1.06	4915 ± 295
Antlia2_215	144.125	−36.7496	11.3 ± 3.5	− 0.04 ± 0.25	5.65 ± 0.37	4672 ± 161
Antlia2_216	144.1626	−36.6182	− 5.3 ± 1.5	− 0.37 ± 0.18	4.16 ± 0.41	4906 ± 151
Antlia2_217	144.8575	−36.4593	300.9 ± 1.1	− 0.72 ± 0.14	4.16 ± 0.24	4377 ± 86
Antlia2_218	144.3082	−36.6104	290.4 ± 2.3	− 1.02 ± 0.2	0.08 ± 0.43	5241 ± 182
Antlia2_219	144.0521	−36.7465	293.0 ± 7.7	− 1.1 ± 0.77	3.83 ± 2.16	5198 ± 386
Antlia2_220	144.4467	−36.6607	284.1 ± 3.1	− 2.33 ± 0.76	3.73 ± 1.05	5019 ± 287
Antlia2_221	144.4118	−36.6823	292.8 ± 0.8	− 1.02 ± 0.15	1.58 ± 0.66	4961 ± 126

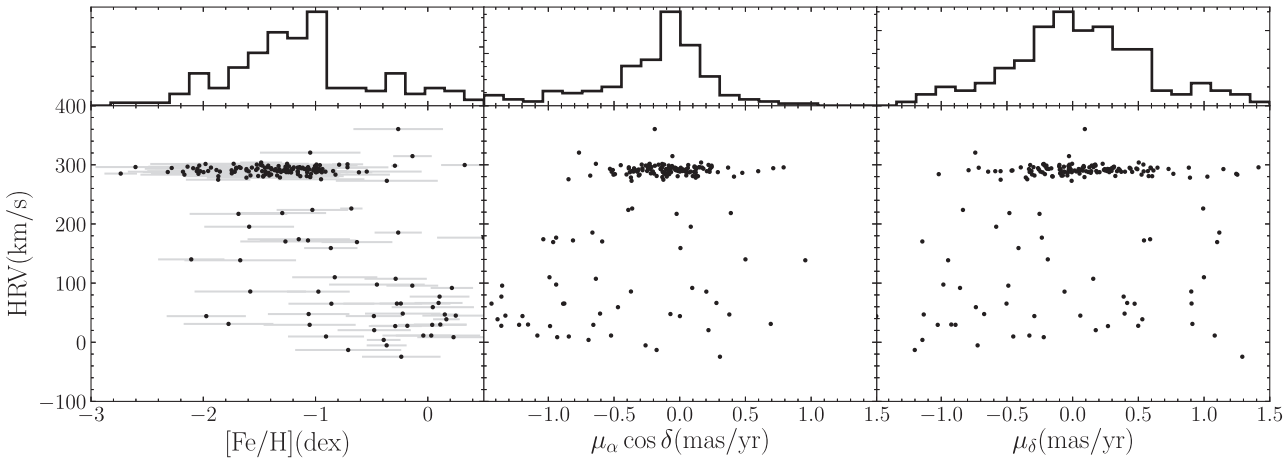

Figure 5. Heliocentric radial velocities of Ant 2 targets. *Left:* HRV versus spectroscopic metallicity. Only stars with good RVs (see Fig. 4) and small metallicity errors $\sigma_{[Fe/H]} < 0.5$ are shown. Ant 2 members stand out clearly as low-metallicity stars, while a small number of foreground contaminants are mostly high-metallicity disc stars. There is also a handful of halo stars. *Middle/right:* HRV versus proper motion in Right Ascension (middle) and Declination (right). Since only stars within ±1.5 mas yr^{-1} were spectroscopically targeted, the proper motion range shown is truncated. Note however that Ant 2's proper motion is clearly distinct from the bulk of the foreground contaminants and concentrates towards $\mu \approx 0$. This can also be seen in the corresponding 1D histograms shown above each panel.

induced either by the internal dynamics in Ant 2 or the perspective 'rotation' effect due to the proper motion of the object (Merritt, Meylan & Mayor 1997; Kaplinghat & Strigari 2008; Walker, Mateo & Olszewski 2008). To test these possible scenarios above we consider the following three models for the systemic velocity V_o of Ant 2:

(i) Constant radial velocity (V_o)
(ii) Radial velocity is a function of systemic velocity, proper motion, and position of the star $V_o = V_o(V_{o,0}, \alpha, \delta, D, \mu_{\alpha,0}, \mu_{\delta,0})$ as predicted by projection effects (perspective rotation).
(iii) The previous model combined with the linear gradient in radial velocity $V_o = V_{o,0} + V_x(\alpha - \alpha_0)\cos\delta_0 + V_y(\delta - \delta_0)$

We also ran the second model using the radial velocity data only, while ignoring the *Gaia* proper motion information in order to separate the inference of Ant 2's proper motion driven by the *Gaia* data from the inference based on the radial velocity gradients.

For all of the three models described above the parameters were sampled using the ensemble sampler. For each posterior sample we ignored the first half of the chain as a burn-in/warm-up. For the remainder of the chains we verified the convergence by checking the acceptance rate across walkers and verified that the means and the standard deviations of the first third of the chains agreed well with the last third part of the chains for each parameter (Geweke & In 1995). The values of common parameters measured from different models mostly agree within 1σ. The parameter values from the model with perspective rotation and no intrinsic velocity gradient such as systemic velocity, proper motions, and velocity dispersion are given in the bottom part of Table 1. The main results are the following: the systemic velocity is $V_o = 290.7 \pm 0.5\,\mathrm{km\,s^{-1}}$, with a velocity dispersion of $\sigma_o = 5.71 \pm 1.08\,\mathrm{km\,s^{-1}}$ and a systemic proper motion of $\mu_\alpha\cos\delta = -0.095 \pm 0.018$ mas yr^{-1}, $\mu_\delta = 0.059 \pm 0.024$ mas yr^{-1}. Note that additional systematic uncertainties of 0.030 and 0.036 for μ_α and μ_δ could be considered, but Ant 2 is not likely to be affected by these systematics as, given its large angular extent, they should average out (Gaia Collaboration 2018b). Also note that we assume a zero binary fraction when estimating the velocity dispersion, which could have the effect of biasing its measurement to slightly higher values (see e.g. Spencer et al. 2017).

The goodness-of-fit (log-likelihood) values for the different models listed above were comparable, with a likelihood ratio of ∼1 – indicating that no very strong evidence for perspective rotation or intrinsic rotation was observed. However the model that was applied to the radial velocity data, while ignoring the *Gaia* proper motions, implied a kinematic proper motion of $\mu_\alpha\cos\delta$, $\mu_\delta = -0.26 \pm 0.13, -0.28 +/- 0.10$ mas yr^{-1}, which is in some tension with the overall (Gaia-based) proper motion of the system. Fig. 6 shows the comparison between the inferred systemic proper motion values, as well as the expected proper motion direction if it was aligned with the orientation of the Antlia 2's iso-density contours. The most likely explanation for the mismatch of the kinematic proper motion and the astrometric proper motion is that Antlia has some intrinsic velocity gradient. This can be associated either with the tidal disruption of the system or with intrinsic rotation.

We have also attempted to measure the velocity dispersion gradient in Antlia 2 by applying the model in equation (2) to stars in three different angular distance bins (with respect to Antlia 2's centre). The bins were selected such that they have an approximately equal number of stars. We kept the parameters of the foreground velocity and the proper motion distribution fixed across those bins and only allowed the velocity dispersion of the dwarf and a mixing

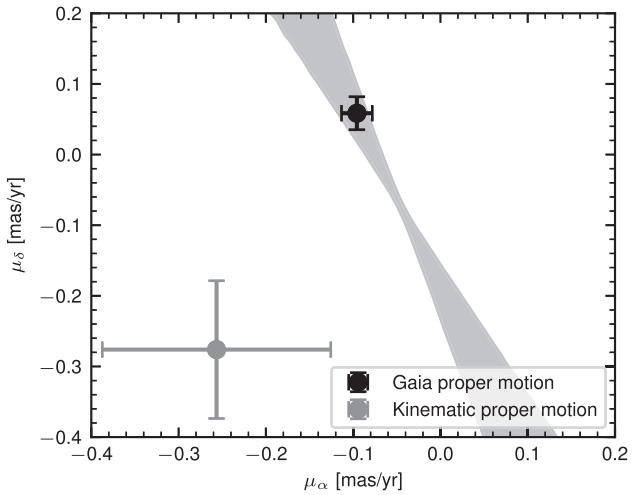

Figure 6. Ant 2's proper motion measurement using two different methods (see main text). The black filled circle shows the proper motion of Ant 2's centre as measured using the *Gaia* DR2 data. The grey filled circle shows the proper motion inferred from the radial velocity gradient (Walker et al. 2006). The grey shaded region shows expected proper motions if Ant 2 moves in the direction indicated by the elongation of Ant 2's iso-density contours, as measured in Section 2.2. The width of the region is driven by uncertainties in Ant 2's distance and iso-density position angle. Note that the *Gaia* proper motion is well aligned with the elongation, suggesting that the elongation may be of tidal nature. The fact that the kinematic proper motions are pointing in a slightly different direction suggests that the dwarf's internal kinematics may be affected by either intrinsic rotation or Galactic tides.

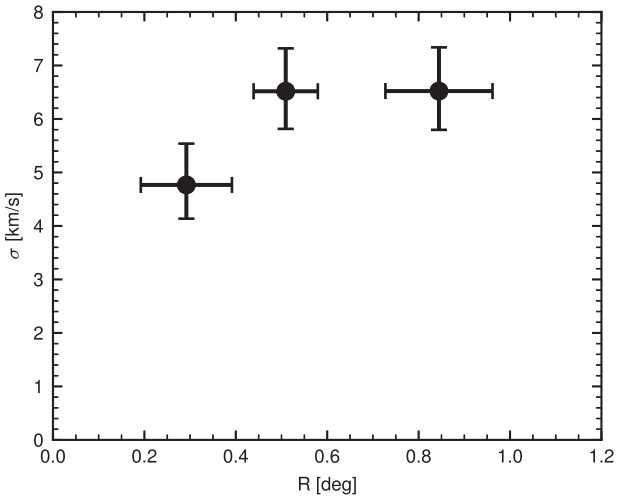

Figure 7. Line-of-sight velocity dispersion measured as a function of radial distance from Ant 2's centre. Each bin contains roughly equal numbers of stars. Error bars correspond to the 16–84 per cent of the measurements. There is a non-statistically significant hint of a velocity dispersion decrease close to the centre.

fraction of dwarf stars to change from bin to bin. The results of this model are shown in Fig. 7. We can see that the velocity dispersion in the very central bin is measured to be somewhat lower than in the outer bins, although by only $\sim 2\sigma$. While the stellar velocity dispersion in a dark matter dominated system can change with radius, there are other possible explanations. Apart from a random fluctuation, this could be due to the existence of a velocity gradient

associated with either rotation or tidal disruption, which would tend to inflate the outer velocity dispersion measurements.

3.2 Orbit

We apply the kinematics of Ant 2 obtained above to gauge the satellite's orbital properties using galpy (Bovy 2015). Motions are converted to the Galactic standard of rest by correcting for the Solar rotation and the local standard of rest velocity, using $v_{\rm circ} = 220\,{\rm km\,s^{-1}}$ and $v_{\rm lsr} = (11.1, 12.24, 7.25)\,{\rm km\,s^{-1}}$ (Schönrich, Binney & Dehnen 2010). Fig. 8 presents the orbit of Ant 2 generated using the *MWPotential2014* (Bovy 2015) with the MW's halo mass increased from 0.8×10^{12} to $0.9 \times 10^{12}\,{\rm M_\odot}$ (see e.g. Vasiliev 2019, for recent mass estimates). The density map in the figure shows the accumulation of the orbits with initial conditions sampled using the uncertainties in radial velocity, proper motions, and distance. The current position of Ant 2 is shown in cyan, and its past and future orbits are shown in black and yellow, respectively. We then estimate the pericentre – using all the sampled orbits – to be at 37^{+20}_{-15} kpc, which is just close enough to induce some tidal disruption in the satellite (see the discussion of the mass measurement of Ant 2 in Section 5). A higher MW mass of 1.8×10^{12} (e.g. Watkins et al. 2019) reduces the median pericentre to $\sim 25^{+13}_{-9}$ kpc, which is around the lower limit of the pericentre uncertainties found for the orbits in a lighter MW (see, however, van der Marel & Guhathakurta 2008, for a possible bias towards larger pericentre values using this method). According to the orbit computed, Ant 2 last passed through pericentre about 1 Gyr ago. It recently crossed the plane of the Galactic disc, but 95 kpc away from the MW centre. The dwarf is about to reach its apocentre. For comparison, the figure also shows the orbit of the LMC (in grey). Both galaxies have similar directions of motion; in fact, Ant 2 is currently sitting very close to where the LMC is heading and where Jethwa, Erkal & Belokurov (2016) predict a large number of low-mass dwarfs stripped from the LMC. However, given the significantly slower orbital velocity of Ant 2 – resulting in a significantly different orbital phase – any obvious association between the two objects seems somewhat unlikely. Fig. 9 illustrates the difference in the orbital paths of the LMC and Ant 2 more clearly.

3.3 Chemistry

We also look at the metallicity distribution of likely members of Ant 2. We select stars within $15\,{\rm km\,s^{-1}}$ of the systemic velocity of Ant 2, small radial velocity error $\sigma_v < 5$ and small uncertainty on [Fe/H] < 0.5 and residual kurtosis and skewness on [Fe/H] less than 1. The stellar metallicity distribution of this sample – which we believe to be free of contamination – is shown in Fig. 10. We note that Ant 2's metallicity peaks at [Fe/H] $= -1.4$, i.e. noticeably higher than the majority of ultra-faint dwarf galaxies. Additionally, the [Fe/H] histogram also shows some moderate asymmetry towards low metallicities, which has been seen in other objects (Kirby et al. 2010). Accordingly, for comparison we overplot the metallicity distributions of a couple of classical dwarf spheroidal galaxies (Leo II and Fornax) from Kirby et al. (2010), whose overall metallicities and MDF shapes are not dissimilar to those of Ant 2. Leo II also has a stellar mass similar to Ant 2's.

To measure the mean metallicity of the system we fit the metallicity distribution by a Gaussian mixture with two Gaussians (due to possible asymmetry of the MDF). In the modelling we take into account abundance uncertainties of individual stars. The resulting mean metallicity is [Fe/H] $= -1.36 \pm 0.04$, with a standard deviation of $\sigma_{\rm [Fe/H]} = 0.57 \pm 0.03$. These measurements are provided in the Table 1. We also note there is a possible abundance gradient with radius, as the subset of stars within 0.5° has a mean metallicity of [Fe/H] $= -1.29 \pm 0.05$ and the stars outside 0.5° have a mean metallicity of [Fe/H] $= -1.44 \pm 0.06$. The difference in metallicities is only marginal, however it is not unexpected, as similar trends with centrally concentrated more metal-rich stellar populations have been observed in many (especially classical) dwarf galaxies (Harbeck et al. 2001; Koch et al. 2006).

4 DISCUSSION

Fig. 11 presents the physical properties of Ant 2 in comparison to other stellar systems in the MW and the Local Group. The left-hand panel shows the distribution of intrinsic luminosities (in absolute magnitudes) as a function of the half-light radius. Strikingly, no other object discovered to date is as diffuse as Ant 2. For example, the so-called ultra diffuse galaxies (van Dokkum et al. 2015) have sizes similar to Ant 2, but are typically ∼6 mag brighter. Overall, compared to systems of similar luminosity, the new dwarf is several times larger, while for objects of comparable size, it is ∼3 orders of magnitude fainter. One exception to this is And XIX (McConnachie et al. 2008), which has had its size updated in Martin et al. (2016b) from 6.2 to 14.2 arcmin. In the figure, we show the old measurement connected with a line to the new measurement. As we can see, And XIX is similar in size to Ant 2, but ∼2 mag brighter. While the half-light radius of And XIX has recently been updated to a much larger value, the available spectroscopy only probes the mass distribution within a much smaller aperture, corresponding to the earlier size measurement. We therefore report a mass measurement for And XIX within 6.2 arcmin but caution the reader against overinterpreting this number. The right-hand panel of the figure shows the satellite's luminosity M_V as a function of the mass within the half-light radius for systems with known velocity dispersion. Here, we have used $M_{\rm dyn} = 581.1\,\sigma_r v^2\,r_{\rm h}$, the mass estimator suggested by Walker et al. (2009). Superficially, Ant 2, although sitting at the edge of the distribution of the currently known dwarfs, does not appear as extreme in the plane of absolute magnitude and mass within the projected half-light radius.

However, the similarity of the Ant 2's mass to that of other dwarfs of comparable luminosity is clearly deceptive. This is because the dwarf's half-light radius is typically an order of magnitude larger than that of other objects at the same level of brightness. Fig. 12 illustrates this by showing the effective density of each satellite, in other words the mass within the half-light radius divided by the corresponding volume. The left-hand panel gives the density as a function of the intrinsic luminosity, while the right panel displays density as a function of the half-light radius. As the figure convincingly demonstrates, Ant 2 occupies the sparsest DM halo detected to date. Interestingly, the dwarf appears to extend the 'universal' density profile suggested by Walker et al. (2009) to lower densities. At the radius probed by Ant 2, the cuspy (blue line) and cored (red line) density profiles start to decouple appreciably. The satellite seems to follow the red curve within the observed scatter. Could the extremely low stellar and DM densities in Ant 2 be the result of the tidal influence of the MW? While the satellite does not come very close to the Galactic centre (as discussed in Section 3.2), at its nominal pericentre of ∼40 kpc, the MW's density is around twice the effective (half-light) density of the object (assuming the

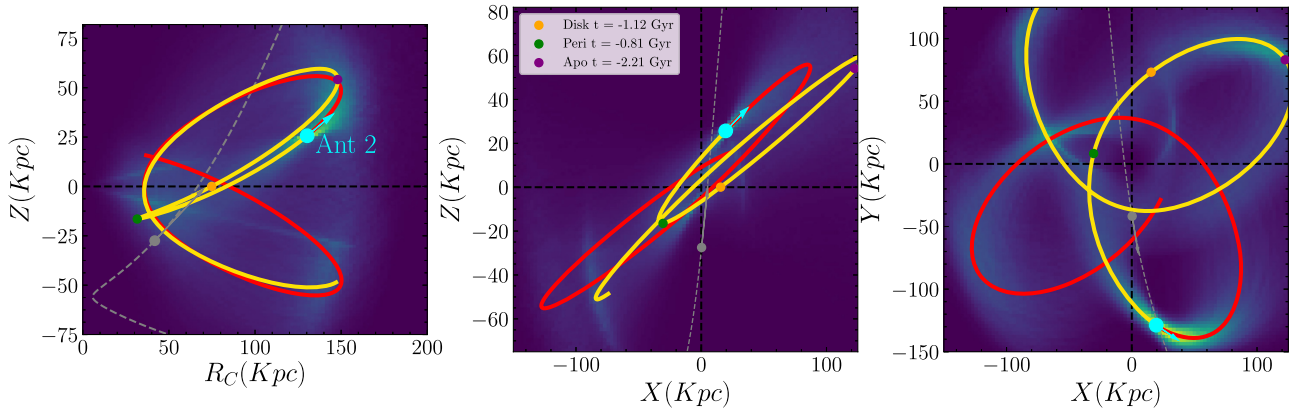

Figure 8. Orbit of Antlia 2 in Galactocentric coordinates. The orbit of Ant 2 is obtained by integrating for 5 Gyr the initial conditions as recorded in Table 1 in the *MWPotential2014* potential from *galpy* (Bovy 2015), but in a DM halo which is 12 per cent more massive. The position of Ant 2 is shown in cyan, together with its past (yellow) and future (red) orbits. The most recent pericentre and apocentre are marked with green and purple filled circles, respectively. The most recent 'disc' crossing is shown in orange. Note that this happens about ∼90 kpc from the centre of the galaxy. The background density map corresponds to the cumulative positions of the orbits sampled according to the uncertainties in the dwarf's line-of-sight velocity, proper motion, and distance. The orbit and position of the LMC are shown in grey. On this orbit, the pericentre of Ant 2 is at 37^{+20}_{-15} kpc.

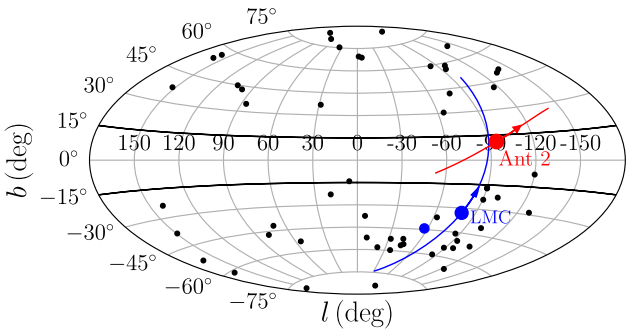

Figure 9. Distribution of the MW dwarf satellites in Galactocentric coordinates (from McConnachie (2012) plus Crater 2 (Torrealba et al. 2016a), Aquarius 2 (Torrealba et al. 2016b), DESJ0225 + 0304 (Luque et al. 2017), Pictor II (Drlica-Wagner et al. 2016), Virgo I (Homma et al. 2016), Cetus III (Homma et al. 2018), Car II and Car III (Torrealba et al. 2018), Hydrus 1 (Koposov et al. 2018), and updated values for the Andromeda galaxies from Martin et al. (2016b)). The position of Ant 2 is shown as a red filled circle. The positions of the Magellanic clouds are shown in blue. Other MW dwarf galaxies are shown in black. The red and blue lines are the orbits of Ant 2 and the LMC, respectively. Black lines enclose the Galactic plane between b ± 15, highlighting the ZOA, which presently clearly shows a dearth of MW satellites. (Note that the black dot closer to the disc corresponds to Canis Major, whose classification as galaxy is uncertain.) Interestingly, while the LMC's orbit is not aligned with that of Ant 2, the new object lies close to the projection of the Cloud's orbital path. Note however that testing the possibility of association between these two objects is not feasible without a detailed simulation of the Magellanic Clouds and Ant 2's accretion onto the MW (see also Fig. 8).

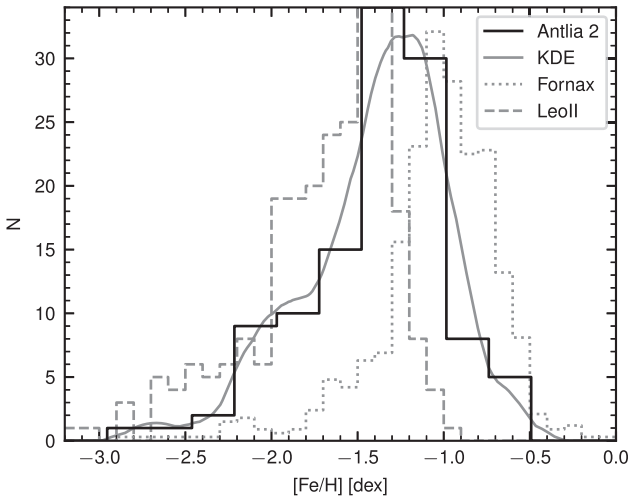

Figure 10. Distribution of spectroscopic metallicities of Ant 2's stars with 274 km s^{-1} < HRV < 303 km s^{-1} and metallicity error less than 0.5 dex. The black line is the [Fe/H] histogram with a bin size of 0.2 dex, while the grey curve shows the kernel density estimation using the Epanechnikov kernel. The mean metallicity is ⟨[Fe/H]⟩ = −1.36, with a significant scatter towards low metallicities. Metallicity distributions of stars in Fornax and Leo II are also shown for comparison.

Galactic mass measurement of Williams et al. 2017)[3], hence some amount of tidal heating/disruption would be expected. Bear in mind however that, while tides tend to lower a satellite's density, typically (as demonstrated by Peñarrubia et al. 2008b, 2012), as the satellite loses mass to the host, it tends to shrink rather than expand. This would imply that the dwarf started with an even *larger* half-light radius (also see Sanders et al. 2018).

There are other indirect hints that Ant 2 might not have escaped the MW's tides. The RRL used to identify the object in *Gaia* DR2 data lie significantly closer to the observer than the dwarf itself, as traced by the RGB and BHB populations (see Section 2.3 for details). The nominal mean distance to these stars is ∼80 kpc, implying that they are some 50 kpc away from the dwarf, signalling extended tidal tails. Moreover, as Fig. 6 illustrates, another clue is the close alignment between the direction of the dwarf's motion (as measured using the GDR2 data, black filled circle with error bars) and the elongation of its iso-density contours (dashed line). In addition, the radial velocity gradient (grey filled circle with error bars) does not fully match the *Gaia* proper motions, possibly indicating

[3]At 20 kpc, the lower 1σ limit of Ant 2's pericentre, the MW density goes up to ∼5 times Ant 2's effective density.

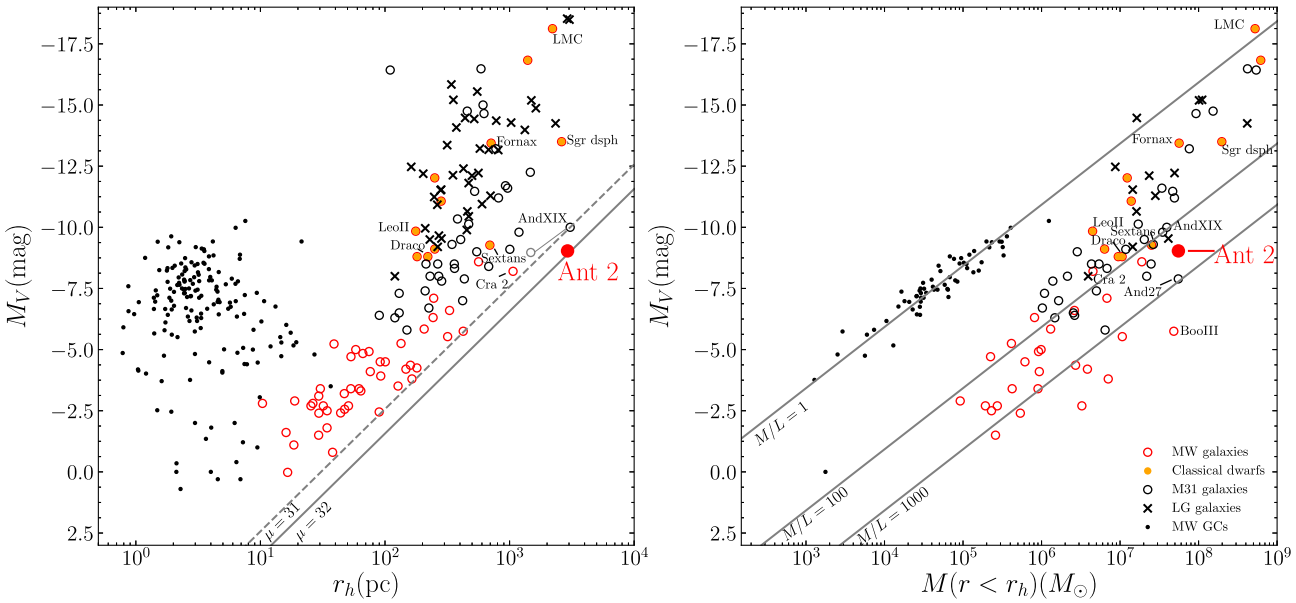

Figure 11. *Left:* Absolute magnitude as a function of half-light radius for galaxies in the Local Group as well as the MW globular clusters. Orange filled circles show the positions of the Classical dwarfs, open red circles give the positions of fainter MW satellites (see Fig. 9 for references to the MW satellite values used) and black dots show the positions of the MW GCs (Belokurov et al. 2010; Harris 2010; Muñoz et al. 2012; Balbinot et al. 2013; Kim & Jerjen 2015; Kim et al. 2015, 2016a; Laevens et al. 2015; Luque et al. 2016, 2017; Martin et al. 2016a; Weisz et al. 2016; Koposov et al. 2017; Luque et al. 2018); the M31 satellites are shown as black open circles and the other LG galaxies are shown as black crosses (both from McConnachie 2012). The position of Antlia 2 is shown with a red filled circle. With a size similar to the LMC, but the luminosity close to that of the faintest of the classical dwarfs, Ant 2 has a surface brightness more than 1 mag fainter than any previously known galaxy. *Right:* Object luminosity as a function of the dynamical mass within the half-light radius. Symbols are the same as in the right panel, but only systems with known velocity dispersions are shown. Masses were estimated using the relation from Walker et al. (2009). The solid grey lines correspond to mass-to-light ratios of 1, 100, and 1000.

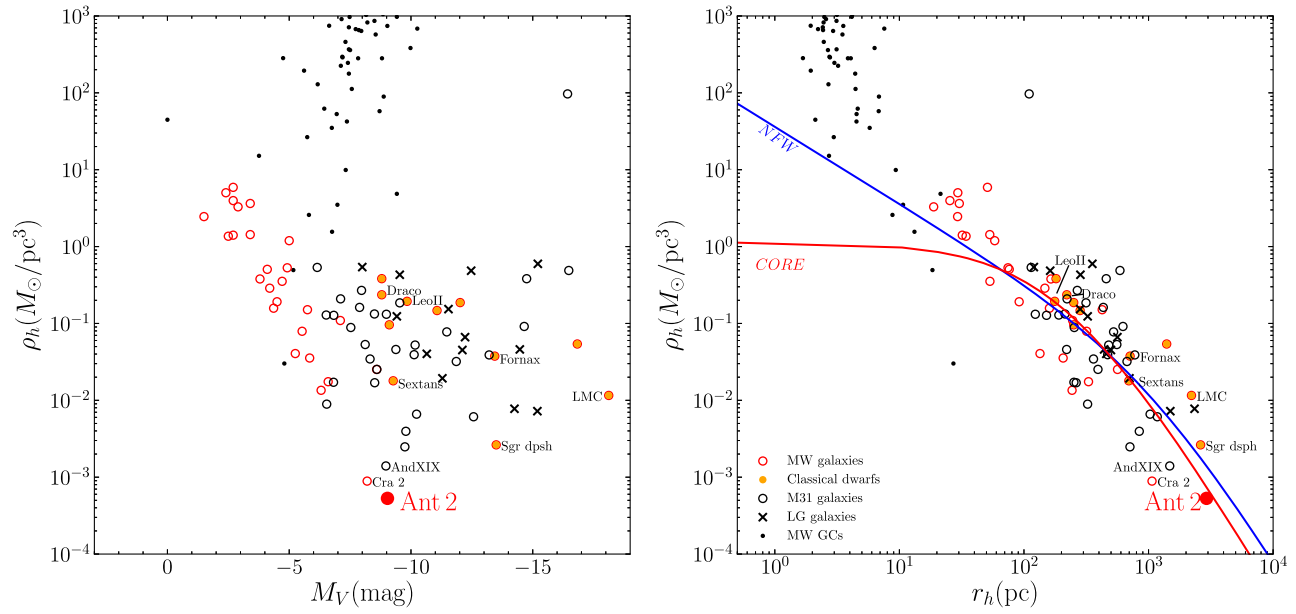

Figure 12. Average (or effective) total matter density within the half-light radius for stellar systems in the LG. Symbols are the same as in Fig. 11. *Left:* Average density as a function of the object's absolute magnitude. A clear selection bias can be seen in the lower left corner of the plot, in which galaxies become too diffuse to be detected. *Right:* Effective density as a function of half-light radius. The blue and red lines are the best-fitting 'universal profiles' for dwarf galaxies from Walker et al. (2009). Blue is an NFW profile, and red corresponds to a cored double power law model. Ant 2 extends the trends reported in Walker et al. (2009) to larger sizes.

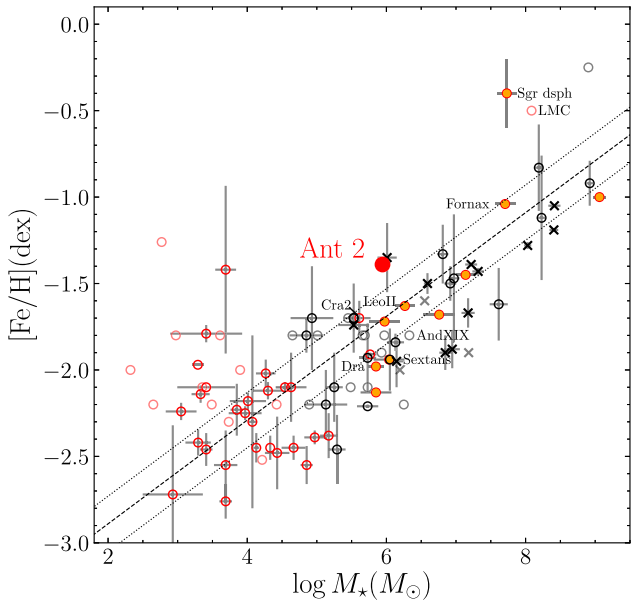

Figure 13. Metallicity as function of stellar mass. The symbols are the same as in Fig. 11. Objects with spectroscopic metallicities are in bold, while those with only photometric measurements are shown as faded symbols. The dashed black line is the mass–metallicity relation from Kirby et al. (2013) with the corresponding 1σ scatter indicated by the dotted lines. Spectroscopic metallicities for dwarf galaxies are from McConnachie (2012), Kirby et al. (2013), Kirby, Simon & Cohen (2015), Kirby et al. (2017b), Caldwell et al. (2017), Torrealba et al. (2016b), Collins et al. (2017), Koposov et al. (2018, 2015b), Li et al. (2018, 2017), Kirby et al. (2017a), Walker et al. (2016), Simon et al. (2017), and Kim et al. (2016b). The remaining photometric data are from the same sources as in Fig. 11.

a velocity field affected by rotation or tides. One can also look for signs of disruption in the mass–metallicity diagram. Fig. 13 shows metallicity as a function of stellar mass for objects in the Local Group. Systems with metallicity inferred from spectroscopy are plotted in full colour, while metallicities deduced from photometry alone are shown as light grey symbols. We have also completely removed objects with metallicities drawn solely based on the colour of the RGB (Da Costa & Armandroff 1990), as these are more affected by systematics due to the age/metallicity degeneracy compared to other photometric methods (see e.g. McConnachie et al. 2008; Kirby et al. 2013, for further discussion). Assuming that a correlation exists between the galaxy's metallicity and its stellar mass – as Fig. 13 appears to indicate – objects that have suffered any appreciable amount of mass-loss would move off the main sequence to the left in this plot. Ant 2 is indeed one such example: while not totally off the mass–metallicity relation, it clearly hovers above it, thus suggesting that some tidal disruption might have occurred. Indeed, if one assumes Ant 2's metallicity originally fit this relation and its metallicity has remained constant, one would expect that Ant 2 should have initially had a stellar mass of $(1 \pm 0.4) \times 10^7\,\mathrm{M}_\odot$, which would imply that today we are seeing only ∼9 per cent of its original population.

4.1 Dark matter halo

Since the Gaia DR2 data do not resolve the internal proper motion distributions within Ant 2, inferences about dynamical mass must rely on the projection of phase space that is sampled by star counts on the sky and spectroscopic line-of-sight velocities. These observations are usefully summarized by the global velocity dispersion, $\sigma_{\rm rv} = 5.7 \pm 1.1$ km s^{-1}, and half-light radius, $R_{\rm h} = 2.86 \pm 0.31$ kpc. On dimensional grounds, the dynamical mass enclosed within a sphere of radius $r = \lambda R_{\rm h}$ can be written

$$M(\lambda R_{\rm h}) = \frac{\lambda\mu}{G} R_{\rm half}\,\sigma_{\rm rv}^2. \tag{3}$$

Equating $\sigma_{\rm rv}$ with the global mean (weighted by surface brightness) velocity dispersion, the coefficient μ depends only on the gravitational potential and the configuration of tracer particles, via the projected virial theorem (Agnello & Evans 2012; Errani, Peñarrubia & Walker 2018):

$$\sigma^2 = \frac{4\pi G}{3}\int_0^\infty r\,\nu(r) M(r)\,\mathrm{d}r, \tag{4}$$

where $\nu(r)$ is the deprojection of the projected stellar density profile; for the adopted Plummer profile, $\nu(r) \propto (1 + r^2/R_{\rm h}^2)^{-5/2}$.

Without invoking a specific mass profile, the simple mass estimator of Walker et al. (2009) effectively assumes $\lambda = 1$ and $\mu = 5/2$, implying for Ant 2 a dynamical mass $M(R_{\rm h}) \approx [5.4 \pm 2.1] \times 10^7\,\mathrm{M}_\odot$ enclosed within a sphere of radius $r = 2.9$ kpc; the quoted uncertainty reflects only the propagation of observational errors, neglecting systematic errors that recent simulations suggest tend to be $\lesssim 20$ per cent regardless of stellar mass (Campbell et al. 2017; González-Samaniego et al. 2017). The more recent estimator of Errani et al. (2018), calibrated to minimize systematics due to uncertainty about the form of the mass profile, uses $\lambda = 1.8$ and $\mu = 3.5$, implying a dynamical mass $M(1.8R_{\rm h}) \approx [1.37 \pm 0.54] \times 10^8\,\mathrm{M}_\odot$ enclosed within a sphere of radius $r = 5.2$ kpc. The corresponding estimator of Campbell et al. (2017) has $\lambda = 1.91$ and $\mu = 3.64$, giving a mass $[1.53 \pm 0.61] \times 10^8\,\mathrm{M}_\odot$ enclosed within a sphere of radius $r = 5.6$ kpc.

In contrast to the use of mass estimators, specification of the stellar number density ($\nu(r)$) and enclosed mass ($M(r)$) profiles lets one use equation (4) to calculate the global velocity dispersion *exactly*. Even though Ant 2's profile might have been modified by its interaction with MW, in order to place Ant 2 in a cosmological context, we first consider the properties of dark matter haloes that might host Ant 2 while following the NFW enclosed-mass profile that characterizes haloes formed in *N*-body simulations (Navarro et al. 1996b; Navarro, Frenk & White 1997):

$$M_{\rm NFW}(r) = 4\pi r_{\rm s}^3 \rho_{\rm s}\left[\ln\left(1 + \frac{r}{r_{\rm s}}\right) - \frac{r/r_{\rm s}}{1 + r/r_{\rm s}}\right]. \tag{5}$$

An NFW halo is uniquely specified by parameters $M_{200} \equiv M(r_{200})$, the mass enclosed within radius r_{200}, inside which the mean density is $\langle\rho\rangle_{200} \equiv 200[3H_0^2/(8\pi G)]$, and concentration $c_{200} \equiv r_{200}/r_{\rm s}$.

For Ant 2 and each of the other Local Group dSphs with measured velocity dispersions and half-light radii (assumed to correspond to Plummer profiles), we use equation (4) to find the parameters of NFW haloes that exactly predict the observed velocity dispersion. For each dwarf, the two degrees of freedom in the NFW profile result in a 'degeneracy curve' of M_{200} as a function of c_{200} (Peñarrubia, McConnachie & Navarro 2008a); in general, higher concentrations require lower halo masses in order to predict the same global velocity dispersion.

The top-left panel of Fig. 14 shows the NFW degeneracy curve for each dwarf galaxy. Given the measured luminosities, and assuming a stellar mass-to-light ratio $\Upsilon_* = 2M_\odot/L_{V,\odot}$, the middle-left panel shows the corresponding relationship between concentration and the ratio of stellar to halo mass, M_*/M_{200}. The bottom-left panel shows

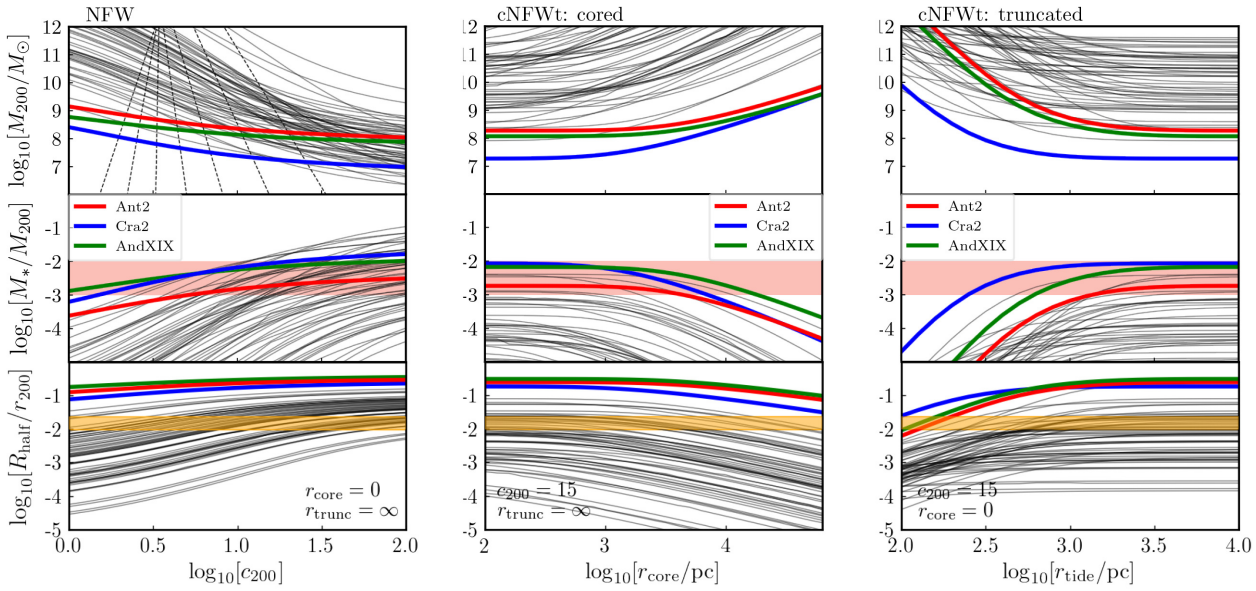

Figure 14. Degeneracy curves showing the relation between dark matter halo properties and halo mass (top), stellar-to-halo mass ratio (middle) and half-light radius to halo radius (bottom), for dark matter haloes constrained by the observed half-light radii and stellar velocity dispersions of individual dwarf spheroidals (one curve per observed dwarf). In the left-hand panels, the haloes are assumed to exactly follow the NFW form, varying only with halo concentration c_{200}. In the middle and right-hand panels, the halo profile is generalized, using equation (6) to allow for modification of an NFW progenitor by the formation of a central core of radius $r_{\rm core}$ or by tidal truncation beyond radius $r_{\rm trunc}$, respectively (in both cases, the halo concentration is held fixed at $c_{200} = 15$). In the top-left panel, dashed lines indicate the halo mass–concentration relations that describe field haloes at redshifts $z = 0, 1, \ldots, 6$ (right to left), derived from the cosmological N-body simulations of Dutton & Macciò (2014). In the middle panels, the salmon shaded region indicates the range of mass ratios where feedback from star formation is expected to transform NFW cusps into cores. In the bottom panels, the orange shaded region represents the relation $\log_{10}[R_{\rm h}/r_{200}] = -1.8 \pm 0.2$, which is expected if half-light radius is determined by halo angular momentum (Kravtsov 2013).

the relationships between concentration and the ratio of half-light radius to the halo radius r_{200}.

We find that Ant 2 joins Crater 2 (Torrealba et al. 2016a) and Andromeda XIX (McConnachie et al. 2008) as extreme objects amongst the Local Group dwarfs. All three are relatively large ($R_{\rm h} \gtrsim 1$ kpc) and cold ($\sigma_{\rm rv} \lesssim 5$ km s^{-1}). As a result, their plausible NFW host haloes tend to have low mass ($M_{200} \lesssim 10^9$ M$_\odot$) even at low concentration. Perhaps most strikingly, all three have extremely large ratios of half-light to halo radius, with $\log_{10}[R_{\rm h}/r_{200}] \gtrsim -1$, putting them $\gtrsim 4\sigma$ above the average relation $\log_{10}[R_{\rm h}/r_{200}] = -1.8 \pm 0.2$ describing sizes of the entire galaxy population in the abundance matching scheme of Kravtsov (2013), suggesting that such a relation might not hold for extreme cases like Ant 2.

Larger halo masses and thus smaller ratios of $R_{\rm h}/r_{200}$ in any of Ant 2, Cra 2, and And XIX would require non-NFW haloes. In general there are two different ways that NFW halo progenitors with more 'normal' values of $M_{200} \gtrsim 10^9$ M$_\odot$ and $\log_{10}[R_{\rm h}/r_{200}] \lesssim -1$ might have been transformed by astrophysical processes into non-NFW haloes that would accommodate the large sizes and small velocity dispersions observed for these galaxies today. The first is the outward migration of central dark matter in response to the rapid loss of gas mass following supernova explosions (e.g. Navarro et al. 1996a; Pontzen & Governato 2012). Recent hydrodynamical simulations demonstrate that such feedback from galaxy formation can turn primordial NFW 'cusps' into 'cores' of near-uniform dark matter density (e.g. Zolotov et al. 2012; Madau, Shen & Governato 2014; Read, Agertz & Collins 2016).

The second mechanism is mass-loss due to tidal stripping, as all three of the extreme objects are satellites of either the Milky Way or M31. Indeed, the orbit inferred from Gaia DR2 proper motions of Crater 2 is consistent with $r_{\rm peri} \lesssim 10$ kpc (see e.g. Fritz et al. 2018), compatible with significant mass-loss. Moreover, Collins et al. (2014) speculate that tidal stripping is the cause of AndXIX's extreme kinematics. In addition to the loss of both dark and (eventually) stellar mass, consequences of tidal stripping include steepening of the outer density profile, shrinking of the luminous scale radius, and reduction of the internal velocity dispersion (Peñarrubia et al. 2008b; Errani et al. 2017).

In order to investigate both of these mechanisms, we consider the generalized 'coreNFWtides' (cNFWt) dark matter halo density model formulated by Read, Walker & Steger (2018), in which the enclosed mass profile is modified from the NFW form according to the following:

$$M_{\rm cNFWt}(r) = \begin{cases} M_{\rm NFW}(r) f^{n_{\rm core}} & r < r_{\rm t} \\ M_{\rm NFW}(r_{\rm t}) f^{n_{\rm core}} + & \\ 4\pi\rho_{\rm cNFW}(r_{\rm t}) \frac{r_{\rm t}^3}{3-\delta} \left[\left(\frac{r}{r_{\rm t}} \right)^{3-\delta} - 1 \right] & r > r_{\rm t} \end{cases} . \quad (6)$$

Here, $f^{n_{\rm core}} \equiv \left[\tanh\left(r/r_{\rm core}\right)\right]^{n_{\rm core}}$ flattens the density profile at radii $r < r_{\rm core}$, generating a more uniform-density core as $n_{\rm core}$ increases from 0 to 1. Beyond the truncation radius $r_{\rm t}$, the density profile steepens from the NFW outer slope of $\rho(r \gg r_{\rm s}) \propto r^{-3}$ to $\rho(r \gg r_{\rm t}) \propto r^{-\delta}$, with $\rho_{\rm cNFW}(r) = f^{n_{\rm core}} \rho_{\rm NFW}(r) + \frac{n^{\rm core} f^{n-1}(1-f^2)}{4\pi r^2 r_{\rm core}} M_{\rm NFW}(r)$ and $\rho_{\rm NFW}(r) = (4\pi r^2)^{-1}\, {\rm d}M_{\rm NFW}/{\rm d}r$.

For each of the observed Local Group dSphs, we again apply equation (4) to find the values of M_{200} that would give the observed global velocity dispersions of these systems. Now, however, we allow the original NFW halo to be modified either by (1) growing a core of radius $r_{\rm core}$ with $n_{\rm core} = 1$, or (2) steepening of the density profile beyond radius $r_{\rm trunc}$ to a log-slope of $-\delta = -5$ (all other parameters in equation 6 are held fixed at NFW values). For

simplicity, we calculate all models holding the concentration fixed at $c_{200} = 15$, a value typical of low-mass dark matter haloes formed in cosmological simulations (Dutton & Macciò 2014). We confirm that alternative choices in the range $10 \leq c_{200} \leq 20$ would not significantly alter the same behaviour in the middle/right columns of Fig. 14.

Representing the processes of core formation and tidal truncation, respectively, the middle and right-hand panels of Fig. 14 display M_{200} and the corresponding ratios $\log_{10}[M_*/M_{200}]$, $\log_{10}[R_h/r_{200}]$ as functions of r_{core} and r_{trunc}. We find that, compared to the unadulterated NFW cases, the observational data can accommodate larger original halo masses when either there forms a core of radius $r_{core} \gtrsim 3$ kpc $\sim R_{half}$, or when tides steepen the density profile beyond radii $r_{trunc} \lesssim 1$ kpc. However, Fig. 14 also indicates that there are problems with both scenarios. The values of r_{core} that would be sufficiently large to give each object a 'normal' half-light to halo radius ratio correspond to M_{200} values so large that the ratio of stellar mass to halo mass plummets, rendering the process of core formation energetically implausible (see Peñarrubia et al. 2012; Di Cintio et al. 2014). Moreover, values of r_{trunc} that would give normal half-light to halo radius ratios correspond to implausibly large progenitor masses of $M_{200} \gtrsim 10^{12}\,M_\odot$ for Ant 2 and And XIX, in which case it would have been the Milky Way and M31 that lost mass to their satellites.

4.2 Tidal evolution

We have found that the properties of Ant 2 are inconsistent with expectations from an isolated NFW halo and proposed two solutions that somewhat alleviate the tension: feedback coring the dark matter profile and tidal disruption. To further investigate these scenarios, we run a series of controlled *N*-body simulations of a dwarf galaxy in the tidal field of the Milky Way. We use the method described in Sanders et al. (2018) to set up the initial conditions for a two-component (dark matter and stars) spherical dwarf galaxy on Ant 2's orbit. We opt for a fixed time-independent axisymmetric Milky Way potential from McMillan (2017),[4] place the dwarf at apocentre $\sim$13 Gyr ago and integrate forwards. In this model, Ant 2 undergoes six pericentric passages. The shape of the orbit is very similar to that shown in Fig. 8 despite the different potential.

We initially selected a $v_{max} = 20\,\mathrm{km\,s^{-1}}$, $c_{200} = 15.9$ NFW halo which is hypothesized to be the lowest mass galaxy-hosting dark matter halo (Okamoto & Frenk 2009). The scale radius of the halo is $r_s = 1.45$ kpc. Choosing a stellar double-power-law density profile with scale radius 1.45 kpc, outer logarithmic slope $\beta = 5$ and transition $\alpha = 2$ and either a core (inner slope $\gamma = 0.1$) or a cusp ($\gamma = 1$) produced similar results: the velocity dispersion fell steadily from $\sim$14 to 8–10 $\mathrm{km\,s^{-1}}$ while the half-light radius fell by $\sim$30 per cent ending at $\sim$1 kpc. Changing the inner stellar and dark matter slope to a more cored $\mathrm{d}\ln\rho/\mathrm{d}\ln r = -0.1$ (while retaining the enclosed central mass), we found that the decay of the velocity dispersion was more rapid (destroying the galaxy on the fifth pericentric passage), while the half-light radius fell more slowly, but could also increase between pericentric passages (as shown in Sanders et al. 2018). We note that these results are largely insensitive to the adopted stellar mass as the stars are subdominant.

[4]Note that for an MW-like galaxy the physical mass growth within $r \sim$ 100 kpc is only 10 per cent in the last $\sim$8 Gyr (see fig. 2 in Wetzel & Nagai 2015). Given the location of Ant 2, the evolution of the MW is thus not likely to be a major concern.

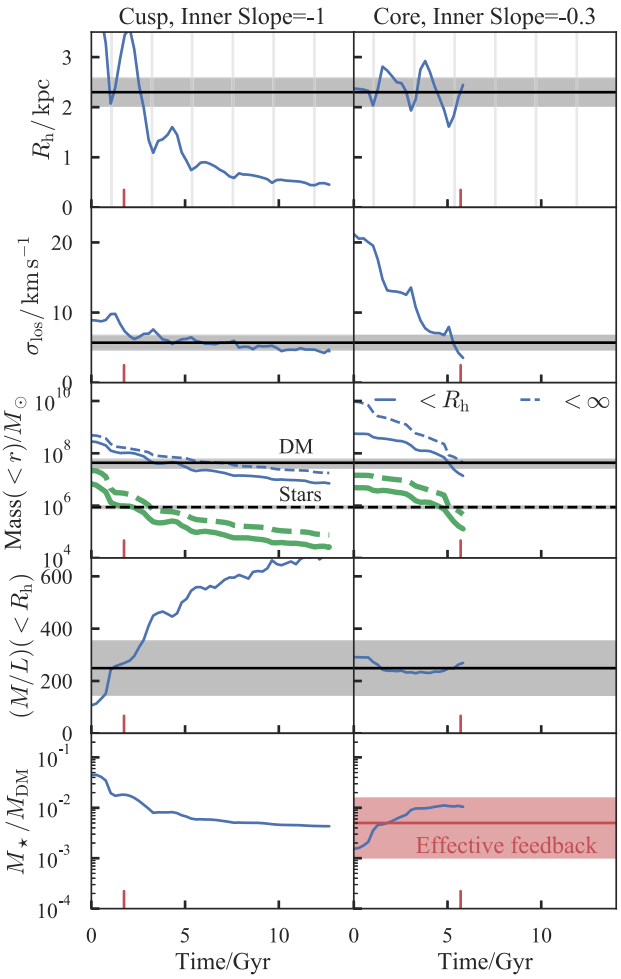

Figure 15. Evolution of two-component *N*-body dwarf galaxy simulations on the orbit of Ant 2: the left column corresponds to a cuspy dark-matter simulation and the right a cored simulation. The four rows show ('circularized') half-light radius, $R_h = r_h\sqrt{b/a}$, velocity dispersion, mass (dark matter in thin blue, stars in thicker green, solid for within R_h, and dashed total), mass-to-light ratio (assuming a stellar mass-to-light ratio of 2.5), and total stellar to dark mass ratio. The black horizontal lines and grey shaded regions give the median and 1σ uncertainty for the corresponding measured properties of Ant 2. The red shaded region in the bottom panel gives the range of mass ratios for which feedback is effective in producing a cored dark matter profile (Bullock & Boylan-Kolchin 2017). The vertical grey lines show the pericentric passages. The red ticks show the times from the two simulations that the observables approximately match Antlia 2.

We have adopted $M_\star = (M_{DM}(<4/3R_h)/(2000\,M_\odot))^{5/3}\,M_\odot$, choosing a stellar mass-to-light ratio of 2.5.

Inspired by these first experiments, we present two scenarios for the evolution of Ant 2: a cuspy dark matter scenario and cored dark matter scenario. The results are shown in Fig. 15. We compute the half-light radius from a Plummer fit to bound particles, and the dispersion is mass-weighted over the entirety of the dwarf (accounting for perspective effects due to Ant 2's large size). For the cuspy model (left column of Fig. 15), we adopt $v_{max} = 16.6\,\mathrm{km\,s^{-1}}$, $c_{200} = 15.9$ producing $r_s = 1.2$ kpc to attempt to match σ_{los}, and set the scale radius of the stars as $r_\star = 7.2$ kpc to attempt to match R_h. Note we are required to set the characteristic stellar radius significantly larger than the dark matter radius, perhaps to an unphysical degree. The dark matter profile is NFW and the stellar

profile has (α, β, γ) = (2, 5, 1). We set the velocity anisotropy of the dark matter as zero and stars as −0.5 (tangential bias). Furthermore, we decrease the mass of stars in the simulation by a factor of 50 to attempt to match the final mass-to-light ratio. We see from Fig. 15 that the final velocity dispersion and mass-to-light ratio match those observed. However, the half-light radius for this model rapidly decays as the model becomes tidally-truncated. Correspondingly, the enclosed masses (both dark and stellar) fail to match those observed. We see that early in the evolution (around 3 Gyr, after a single pericentric passage) the simulation matches all observables well. However, the simulation shows that a stellar profile that extends significantly beyond the scale radius of the dominant dark matter mass component is rapidly truncated by tides and such configurations only last a few orbital periods. In conclusion, a cuspy model can reproduce the observables but only with a contrived low-mass dark matter halo and a highly extended stellar profile. Such a configuration is rapidly destroyed by the Milky Way's tidal field.

As the cuspy model fails to adequately produce all the observables under reasonable assumptions, we attempt to produce a cored model that satisfactorily explains the data. We start with $v_{\rm max} = 37.4\,{\rm km\,s^{-1}}$, $c_{200} = 15.9$ producing $r_{\rm s} = 2.7$ kpc and set the stellar and dark matter inner slope as $\mathrm{d}\ln\rho/\mathrm{d}\ln r = -0.3$ (retaining the enclosed central mass) – this produces a slope of $\mathrm{d}\ln\rho/\mathrm{d}\ln r \approx -0.8$ at 1.5 per cent of $R_{\rm vir}$. We set the scale radius of the stars as $r_\star = r_{\rm s}$ (a more reasonable assumption than our overextended cuspy model) and decrease the mass of stars by a factor of ∼250. We use the same outer slopes, transition slopes and velocity anisotropies as the cuspy case. From the right column of Fig. 15 we find the dispersion falls rapidly, with the dwarf only surviving three pericentric passages. After the third pericentric passage the dwarf has a dispersion similar to that of Ant 2. Between pericentric passages the half-light radius inflates slightly but stays approximately constant and consistent with the data. The total stellar mass to dark mass ratio increases by nearly an order of magnitude whilst the mass-to-light ratio stays approximately constant over the simulation. There is a compromise between producing an initial total stellar to dark-matter mass ratio that is high enough to yield cored profiles via feedback ($M_\star/M_{\rm DM} \sim 0.001-0.015$, Di Cintio et al. 2014; Bullock & Boylan-Kolchin 2017) and a high enough mass-to-light ratio to match that observed for Ant 2. However, there is some freedom in our choice of stellar mass-to-light ratio, which was set at 2.5 but could be larger for a steeper low-mass initial mass function slope (e.g. Salpeter). Interestingly, the heavy tidal disruption scenario requires an initial stellar mass in the model of $\sim 1 \times 10^7\,{\rm M_\odot}$, placing the progenitor of Ant 2 on the mass–metallicity relation of the other dwarf galaxies in Fig. 13. Furthermore, heavy tidal disruption is also accompanied by sphericalization of the dwarf galaxy (Sanders et al. 2018) which is possibly in contradiction with the observed stellar axial ratio of ∼0.6. However, further simulations of flattened progenitors are needed to confirm whether this is a significant issue.

A prediction of the cored scenario is that the dwarf galaxy has deposited ∼90 per cent of its stellar mass into the Milky Way halo. In Fig. 16 we show the expected surface brightness of the resulting material (typically 34–35 mag arcsec^{-2}) as well as the expected median distances and proper motions using the final apocentric passage from the simulation rotated to the present coordinates of Ant 2. The line-of-sight distribution of the tidal debris in this simulation is shown in Fig. 17. Given the current dwarf's location near the apocentre, a substantial portion of the debris is distributed along the line of sight, extending as far as 50 kpc from the progenitor towards the Sun. It appears that, given *Gaia's* bright limiting magnitude for detecting RRL stars (dashed line), only the near side of the debris cloud can be detected using the RRL catalogue discussed above (as illustrated by the dashed line and the filled black circles). If our interpretation is correct, then the three RRL detected are only a small fraction of the dwarf's total cohort of such stars; as noted above, the existence of a much larger undetected population of RRL would be consistent with recent results obtained for the Crater 2 dwarf (Joo et al. 2018; Monelli et al. 2018), which is of comparable total luminosity. Our cored simulation predicts ∼250 RRL within a 20 × 20 deg box of Ant 2 (assuming Gaia observes all RRL out to 90 kpc – a limiting magnitude of $G = 20.27$), whilst the cuspy simulation predicts almost 28 000! At the representative time we have chosen for the cuspy simulation, the tidal disruption is not significant enough to explain the observed foreground RRL, lending support to the cored picture.

In conclusion, we have found that the only cuspy profiles that adequately explain the data have both haloes with smaller $v_{\rm max}$ than that required to explain most other dwarf galaxies, and stellar profiles that extend further than the effective radius of the dark halo ($R_{\rm h}/r_{\rm s} \sim 2$). Such an already unlikely configuration does not survive long within the tidal field of the Milky Way, as the exposed stellar profile becomes heavily truncated. However, a cored dark matter profile more naturally explains the data. In this scenario, Ant 2 is embedded initially in a larger, more massive dark matter halo which naturally produces a broader stellar distribution. The dwarf is then heavily tidally disrupted by the Milky Way's tidal field such that, after a few pericentric passages, the velocity dispersion has fallen to the observed value while the half-light radius is unchanged. In this picture, Ant 2 has deposited a large fraction of its stellar mass onto the Milky Way, possibly explaining the foreground RRL, and is expected to fully disrupt during the next pericentric passage.

It is not wholly evident whether the formation of such a large core is consistent with feedback. Although the slope of the density profile close to the centre can be reproduced in some feedback models (Tollet et al. 2016), it is unclear whether such a large core size is really attainable. There remain other possibilities for the formation of cores in dwarf galaxies, including the solitonic cores formed in ultralight scalar dark matter particle theories (Schive, Chiueh & Broadhurst 2014; Hui et al. 2017). This theory has had some success with reproducing smaller, but kiloparsec-sized, cores in the classical dwarf galaxies (Schive et al. 2014, 2016). Self-interacting dark matter (SIDM), in which the cross-section of interaction of the DM particles is velocity dependent, can also produce cores. These are typically of the size of ∼1 kpc (Tulin & Yu 2018), though they need some fine-tuning of the value of the ratio of velocity dispersion to DM particle mass. It is an open question whether a large core can be produced in a low-density and low-velocity dispersion DM halo by SIDM theories. Given the multiple populations seen in the extended metallicity distribution function of Fig. 10, the acquisition of further line-of-sight velocities will enable the DM density to be mapped out using the methods of Walker & Peñarrubia (2011) and Amorisco & Evans (2012). This may enable us to confirm the existence of a core directly from the data, as well as to measure its size. This should help resolve whether Ant 2 is completely consistent with the predictions of feedback, and perhaps even constrain alternative dark matter theories such as SIDM.

4.3 Dark matter annihilation

Like other Milky Way dwarf spheroidal galaxies, Ant 2 is a potential target for gamma-ray searches for dark matter annihilation (e.g. Bertone, Hooper & Silk 2005; Geringer-Sameth, Koushiappas &

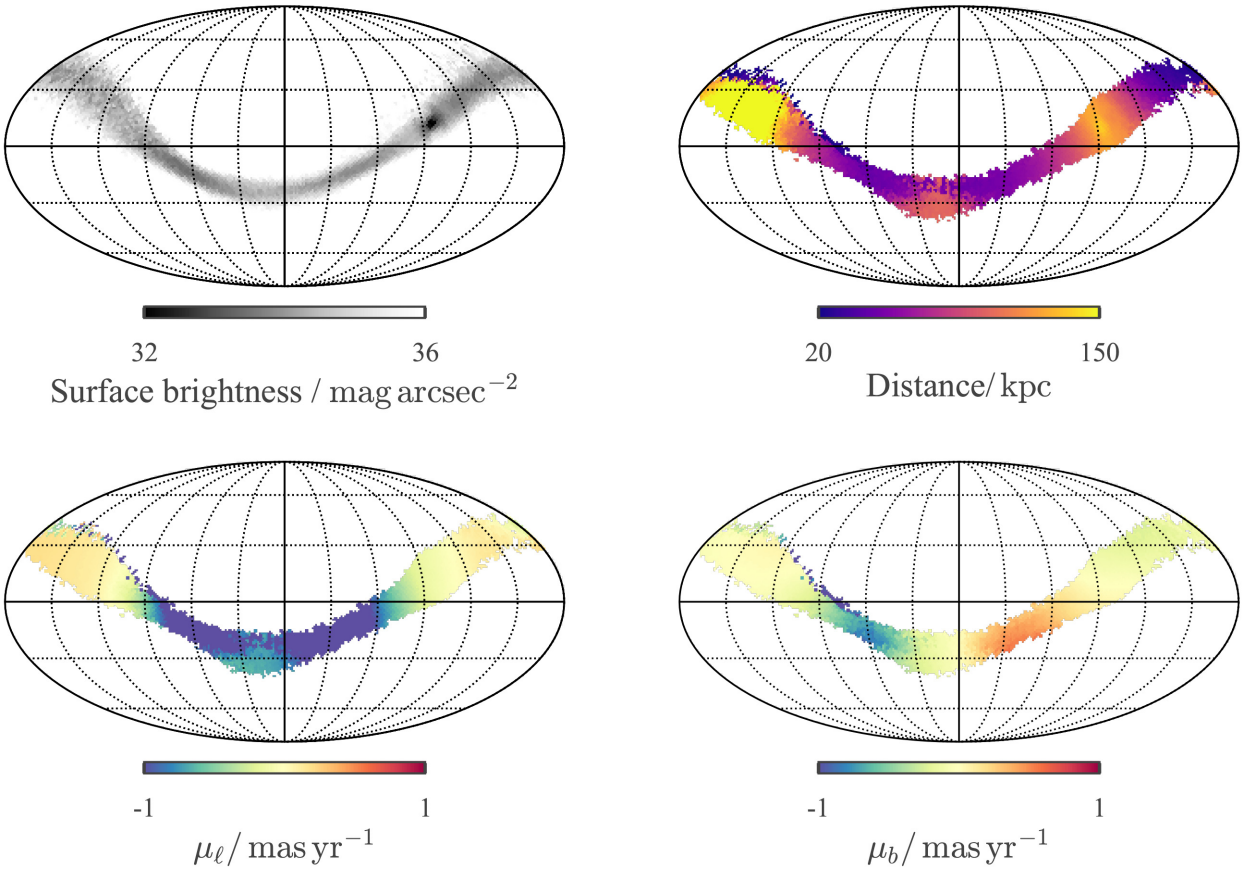

Figure 16. Simulation of Ant 2's disruption on the sky in Galactic coordinates: the four panels show the surface brightness, mean distance and galactic proper motions for the cored simulation in the left-hand column of Fig. 15.

Walker 2015a and references therein). In particular, the dwarfs' old stellar populations and lack of gas make them very unlikely to emit gamma-rays through conventional processes. For dark matter particles with mass in the GeV to TeV range, searches in dwarfs with the Fermi Large Area Telescope (Atwood et al. 2009) are among the most sensitive probes of dark matter annihilation (e.g. Albert et al. 2017).

Ant 2's small velocity dispersion for its size indicates a low-density dark matter halo (see previous two sub-sections for details), and since the gamma-ray flux from annihilation is proportional to the square of the dark matter density, Ant 2 would likely have quite a low signal compared with other dwarfs. Using the simple estimator in equation 8 of Evans, Sanders & Geringer-Sameth (2016) and the properties of Ant 2 in Table 1 we compute the total flux from dark matter annihilating within 0.5° of the centre of Ant 2. Assuming a dark matter halo with a $\rho \propto r^{-1}$ density profile[5] we find $\log_{10}J(0.5^\circ)/(\mathrm{GeV^2\,cm^{-5}}) \approx 16 \pm 0.4$, where J is proportional to the gamma-ray flux. This is about 3 orders of magnitude below the J values of the 'top tier' Milky Way dwarfs where we expect the strongest annihilation signals (e.g. Bonnivard et al. 2015).

Although we do not expect a detectable annihilation signal from Ant 2 an exploration of the Fermi data illustrates a number of issues that will confront future searches in such large objects. First, Ant 2 may be significantly extended as seen by Fermi. Dark matter haloes are generally less concentrated than the stars they host and, in contrast with other dwarfs, Ant 2's stellar half-light angle is already much larger than Fermi's PSF. We create surface brightness profiles for dark matter emission and convolve them with Fermi's (energy-dependent) PSF. The size of Ant 2 as seen by Fermi can be characterized by the angle at which the PSF-convolved surface brightness drops to half its maximum value. We find the ratio between this angle and the corresponding angle for a point source of gamma rays. The most point-like situation we consider is a spherical NFW halo with scale radius twice the half-light radius[6] and which is truncated beyond the scale radius. For 1 GeV gamma rays Ant 2 is 50 per cent more extended than a point source (80 per cent at 10 GeV). For less cuspy density profiles the extension is more pronounced: a modified NFW profile with $\rho \propto r^{-0.5}$ in its inner parts yields emission at 1 GeV that is 2.4 times more extended than a point source (4.3 times more at 10 GeV). The shape of Ant 2's halo is quite uncertain and so a simple search for a gamma-ray point source may not be optimal. Nevertheless, an eventual detection of spatially extended emission is quite powerful as it would yield a direct observation of the halo density profile (e.g. Geringer-Sameth, Koushiappas & Walker 2015b).

We prepare data from 9.4 yr of Fermi observations using the procedure described by Koposov et al. (2018) except that we include

[5]The J value increases by no more than 0.4 dex when varying the logarithmic slope of the density profile between −0.6 and −1.4.

[6]We use the 'circularized' half-light radius $r_\mathrm{h}\sqrt{b/a} = 2.3$ kpc.

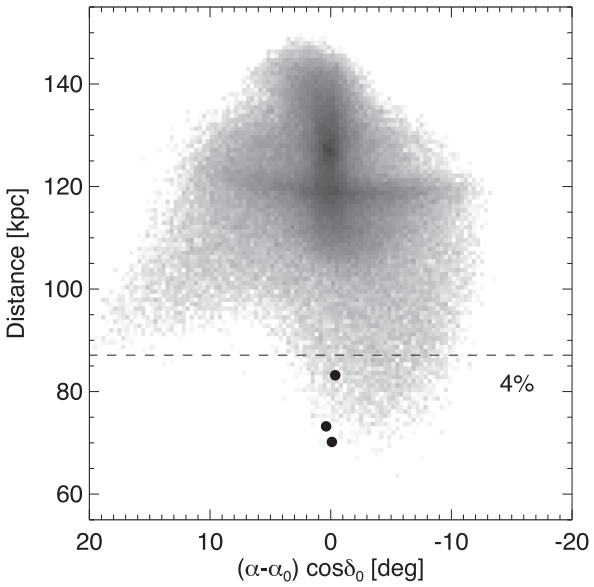

Figure 17. Line-of-sight distance distribution of tidal debris at the present day for the cored simulation in the right column of Fig. 15 as a function of RA (for the same extent in Dec.). The dashed line gives the tentative RRL detection limit for *Gaia*. As indicated in the figure, only 4 per cent of the total number of RRL in this (large) area of the sky are below the dashed line and thus are bright enough to be detectable by *Gaia*. The filled black circles indicate the locations of the three RRL with $D_{\rm h} > 70$ kpc coincident with the dwarf's location on the sky. The horizontal stripes at $D_{\rm h} \approx 120$ kpc and $D_{\rm h} \approx 130$ kpc are the ends of the leading and trailing debris from the penultimate pericentric passage.

energies from 0.5 to 500 GeV and consider the region within a 20° square centred on Ant 2. As in the above study we fit a model to the region using maximum likelihood (the model includes isotropic and Galactic diffuse emission and point sources from the Third Fermi Source Catalogue, Acero et al. 2015). Fitting an additional trial point source with a flexible energy spectrum at the location of Ant 2 does not improve the fit ($2\Delta\log L = 0.75$, where L is the Poisson probability of obtaining the data given the model). We also examine the energy spectra of events within various-sized apertures centred on Ant 2 as compared to the background model and find no significant bumps or discrepancies.

As a way of checking for extended emission we rebin the counts and model maps from the original 0.05° pixelization into coarser maps with 0.25°, 0.5°, 1°, and 1.5° pixels (where the central pixel is always centred on Ant 2). In each pixel p we construct a statistic to measure the discrepancy with the best-fitting background model: $\chi^2_p = \sum(c_{pi} - m_{pi})^2/m_{pi}$, where c_{pi} and m_{pi} are the observed and expected numbers of counts in pixel p and energy bin i and the sum is taken over energy bins between 1 and 10 GeV. Generating sky maps based on χ^2_p yields no 'hot spots' centred on Ant 2.

One major caveat is that the Galactic diffuse template provided by the Fermi Collaboration already absorbs extended excess emission on scales larger than about 2° (Acero et al. 2016), and so it is possible that Ant 2 has already been included in the background model. We examine the morphology of the diffuse template and do not find any blob-like emission centred on Ant 2, though this is somewhat difficult due to Ant 2's proximity to the Galactic plane, a region with numerous diffuse structures and gradients. In order to try to suppress the very bright emission from the Galactic plane we re-extract the data but keep only `PSF3` events.[7] This subset of data is roughly the quarter of events with the best direction reconstruction. While this will not help detect extended emission it does reduce the glare from the Galactic plane. Examining the `PSF3` counts maps reveals two potential point sources within the half-light ellipse of Ant 2, $\Delta\ell = 0.3^\circ$, $\Delta b = -0.3^\circ$ away from the centre of the dwarf. Fitting point sources at these locations gives an improvement of $2\Delta\log L = 17$. However, this comes at the cost of greatly increased model complexity and so the resulting significance of these potential sources (p value) is only around the 5 per cent level. In any case a dark matter explanation would require a density profile significantly offset from the stellar distribution.

Despite the lack of a signal from Ant 2, its huge angular size hints at a possible opportunity for gamma-ray searches using dwarfs. The most powerful dark matter searches combine observations of multiple dwarfs by assigning weights to the gamma-ray events from each dwarf (Geringer-Sameth & Koushiappas 2011; Geringer-Sameth et al. 2015a). For the optimal set of weights, each dwarf contributes to the expected signal to noise in quadrature as $\mathrm{SNR}^2 = \sum s^2/b$, where the sum runs over energy and spatial bins, and s and b are the expected number of dark matter photons and background events detected in each (generally infinitesimal) bin (see equation 18 of Geringer-Sameth et al. 2015a). For dwarfs with identical dark matter haloes, as long as the spatial extent of the emission is smaller than the PSF, a dwarf's contribution to SNR^2 is proportional to $1/D^4$ (the amplitude of s scales as the total flux $1/D^2$ while the shape of s is fixed by the PSF). For a homogeneous distribution of dwarfs (number density $\propto D^2\,\mathrm{d}D$), this scaling leads to searches dominated by the nearest dwarfs, e.g. Ursa Major II, Coma Berenices, and Segue 1. In contrast, for dwarfs with extended emission SNR^2 scales as $1/D^2$ (in this case the amplitude of s is fixed but the shape of the surface brightness profile contracts by a factor of $1/D$). If Ant 2 is the first of many 'missing giants' we may eventually find ourselves with an abundance of relatively distant, spatially extended gamma-ray targets. Since $J \propto \sigma_v^4/r_{\rm h}$ (Evans et al. 2016), such dwarfs will be especially important if they have larger velocity dispersions and/or smaller half-light radii than Ant 2 (as is perhaps suggested by the isolated position of Ant 2 in Fig. 11). It may turn out that this large population becomes as important for constraining dark matter particles as the handful of 'point source-like' dwarfs that are currently the most informative.

5 CONCLUSIONS

We have presented the discovery of a new dwarf satellite galaxy of the Milky Way, Antlia 2 (Ant 2). Originally detected in *Gaia* DR2 data using a combination of RRL, proper motions, parallaxes and shallow broad-band photometry, this new satellite is also confirmed using deeper archival DECam imaging as well as AAT 2dF + AAOmega follow-up spectroscopy. The CMD of the Ant 2 dwarf boasts a broad and well-populated RGB as well as a prominent BHB sequence, which we use as a standard candle. The resulting dwarf's distance modulus is $m - M = 20.6$, which is consistent with the location of the RGB, giving an independent confirmation of the BHB distance. In addition, there are possibly three associated RRL stars, lying in front of the dwarf along the line of sight. These likely represent the near side of an extended cloud of tidal debris originating from Antlia 2. The angular half-light radius of the new

[7] https://fermi.gsfc.nasa.gov/ssc/data/analysis/documentation/Cicerone/Cicerone_Data/LAT_DP.html

dwarf is ∼1.3°, which translates into a gigantic physical size of ∼2.8 kpc, on par with the measurements of the largest satellite of the MW, the LMC, but with a luminosity some ∼4000 times fainter.

Using ∼200 spectroscopically confirmed RGB member stars, we have measured the dwarf's velocity dispersion to be ∼5.7 km s^{-1}, which, combined with the luminosity $M_V = -9$, yields a high mass-to-light ratio of ∼300, typical for a Galactic dwarf. However, given Ant 2's enormous size, the implied effective DM density is much lower than that of any other dwarf satellite studied to date. Assuming an NFW density profile, Ant 2 is hosted by a relatively light DM halo with $M_{200} < 10^9$ $M_\odot$ – close to the lowest mass inferred for the Galactic dwarfs (see Jethwa, Erkal & Belokurov 2018) – which is not easy to reconcile with its grotesquely bloated appearance. Even if the DM density deviates from the canonical NFW shape – be it either due to the effects of stellar feedback or of the Milky Way's tides – bringing the object's half-light radius in accordance with the rest of the Galactic satellite population appears difficult.

None the less, a combination of feedback and tides working in concert may provide a plausible way to explain the observed properties of Ant 2. This solution requires a substantially more luminous dwarf to be born in a (i) relatively massive and (ii) cored DM halo, which subsequently suffers prolific tidal stripping. We have shown that for such a cored host, the half-light radius changes little during the disruption but the velocity-dispersion plummets. A strong prediction of this model is a large amount of tidal debris left behind by Ant 2, which could be tested by surveying (with either imaging or spectroscopy) the area around the dwarf. Note however, that even in this scenario, the structural properties of Ant 2's progenitor remain extreme. For example, in the size–luminosity plane shown in Fig. 11, it must have occupied the empty space below and to the right of Sgr, with $r_h \sim 3$ kpc and $M_V \sim -12$.

Given that it currently appears impossible for Ant 2 to be born with a half-light radius much smaller than currently measured, its position on the size–luminosity plane (even extrapolated back in time) may imply that dwarf galaxy formation can proceed at surface brightness (and density) levels significantly lower than those so far observed. Hence Ant 2 could be the tip of an iceberg – a population of extremely diffuse Galactic dwarf galaxies even fainter than the numerous satellites detected in wide-area photometric surveys over the past two decades. Fortunately, Gaia data – as illustrated by this work – may be the key to testing this hypothesis.

ACKNOWLEDGEMENTS

It is a pleasure to thank Andrey Kravtsov and Jorge Peñarrubia for enlightening discussions that helped to improve the quality of this manuscript, and Chris Lidman for carrying out the spectroscopic service observations on the AAT. The authors thank Gisella Clementini and Vincenzo Ripepi for pointing out an error in the RRL luminosity calculation in an earlier version of this manuscript. The anonymous referee is thanked for many helpful comments.

This project was developed in part at the 2018 NYC Gaia Sprint, hosted by the Center for Computational Astrophysics of the Flatiron Institute in New York City. The research leading to these results has received funding from the European Research Council under the European Union's Seventh Framework Programme (FP/2007-2013) / ERC Grant Agreement n. 308024. SEK and MGW are supported by National Science Foundation grant AST-1813881. GT acknowledges support from the Ministry of Science and Technology grant MOST 105-2112-M-001-028-MY3, and a Career Development Award (to YTL) from Academia Sinica.

This work presents results from the European Space Agency (ESA) space mission Gaia. Gaia data are being processed by the Gaia Data Processing and Analysis Consortium (DPAC). Funding for the DPAC is provided by national institutions, in particular the institutions participating in the Gaia MultiLateral Agreement (MLA). The Gaia mission website is https://www.cosmos.esa.int/gaia. The Gaia archive website is https://archives.esac.esa.int/gaia.

This paper includes data gathered with Anglo-Australian Telescope at Siding Spring Observatory in Australia. We acknowledge the traditional owners of the land on which the AAT stands, the Gamilaraay people, and pay our respects to elders past and present.

This project used data obtained with the Dark Energy Camera (DECam), which was constructed by the Dark Energy Survey (DES) collaboration. Funding for the DES Projects has been provided by the U.S. Department of Energy, the U.S. National Science Foundation, the Ministry of Science and Education of Spain, the Science and Technology Facilities Council of the United Kingdom, the Higher Education Funding Council for England, the National Center for Supercomputing Applications at the University of Illinois at Urbana-Champaign, the Kavli Institute of Cosmological Physics at the University of Chicago, the Center for Cosmology and Astro-Particle Physics at the Ohio State University, the Mitchell Institute for Fundamental Physics and Astronomy at Texas A&M University, Financiadora de Estudos e Projetos, Fundação Carlos Chagas Filho de Amparo à Pesquisa do Estado do Rio de Janeiro, Conselho Nacional de Desenvolvimento Científico e Tecnológico and the Ministério da Ciência, Tecnologia e Inovacão, the Deutsche Forschungsgemeinschaft, and the Collaborating Institutions in the Dark Energy Survey.

The Collaborating Institutions are Argonne National Laboratory, the University of California at Santa Cruz, the University of Cambridge, Centro de Investigaciones Enérgeticas, Medioambientales y Tecnológicas-Madrid, the University of Chicago, University College London, the DES-Brazil Consortium, the University of Edinburgh, the Eidgenössische Technische Hochschule (ETH) Zürich, Fermi National Accelerator Laboratory, the University of Illinois at Urbana-Champaign, the Institut de Ciències de l'Espai (IEEC/CSIC), the Institut de Física d'Altes Energies, Lawrence Berkeley National Laboratory, the Ludwig-Maximilians Universität München and the associated Excellence Cluster Universe, the University of Michigan, the National Optical Astronomy Observatory, the University of Nottingham, the Ohio State University, the University of Pennsylvania, the University of Portsmouth, SLAC National Accelerator Laboratory, Stanford University, the University of Sussex, and Texas A&M University.

REFERENCES

Acero F. et al., 2015, ApJS, 218, 23
Acero F. et al., 2016, ApJS, 223, 26
Agnello A., Evans N. W., 2012, ApJ, 754, L39
Albert A. et al., 2017, ApJ, 834, 110
Amorisco N. C., Evans N. W., 2012, MNRAS, 419, 184
Antoja T. et al., 2015, MNRAS, 453, 541
Atwood W. B. et al., 2009, ApJ, 697, 1071
Baker M., Willman B., 2015, AJ, 150, 160
Balbinot E. et al., 2013, ApJ, 767, 101
Belokurov V. A., Erkal D., 2019, MNRAS, 482, L9
Belokurov V. et al., 2010, ApJ, 712, L103
Bertone G., Hooper D., Silk J., 2005, Phys. Rep., 405, 279
Bonnivard V. et al., 2015, MNRAS, 453, 849
Bose S., Deason A. J., Frenk C. S., 2018, ApJ, 863, 123
Bovy J., 2015, ApJS, 216, 29

Bressan A., Marigo P., Girardi L., Salasnich B., Dal Cero C., Rubele S., Nanni A., 2012, MNRAS, 427, 127
Bullock J. S., Boylan-Kolchin M., 2017, ARA&A, 55, 343
Bullock J. S., Stewart K. R., Kaplinghat M., Tollerud E. J., Wolf J., 2010, ApJ, 717, 1043
Caldwell N. et al., 2017, ApJ, 839, 20
Campbell D. J. R. et al., 2017, MNRAS, 469, 2335
Chabrier G., 2003, PASP, 115, 763
Chan T. K., Kereš D., Wetzel A., Hopkins P. F., Faucher-Giguère C.-A., El-Badry K., Garrison-Kimmel S., Boylan-Kolchin M., 2018, MNRAS, 478, 906
Clementini G. et al., 2019, A&A, 622, A60
Collins M. L. M., Tollerud E. J., Sand D. J., Bonaca A., Willman B., Strader J., 2017, MNRAS, 467, 573
Collins M. L. M. et al., 2014, ApJ, 783, 7
Da Costa G. S., Armandroff T. E., 1990, AJ, 100, 162
Deason A. J., Belokurov V., Evans N. W., 2011, MNRAS, 416, 2903
Di Cintio A., Brook C. B., Dutton A. A., Macciò A. V., Obreja A., Dekel A., 2017, MNRAS, 466, L1
Di Cintio A., Brook C. B., Macciò A. V., Stinson G. S., Knebe A., Dutton A. A., Wadsley J., 2014, MNRAS, 437, 415
Drlica-Wagner A. et al., 2016, ApJ, 833, L5
Dubinski J., Carlberg R. G., 1991, ApJ, 378, 496
Dutton A. A., Macciò A. V., 2014, MNRAS, 441, 3359
El-Badry K., Wetzel A., Geha M., Hopkins P. F., Kereš D., Chan T. K., Faucher-Giguère C.-A., 2016, ApJ, 820, 131
El-Zant A., Shlosman I., Hoffman Y., 2001, ApJ, 560, 636
Errani R., Peñarrubia J., Laporte C. F. P., Gómez F. A., 2017, MNRAS, 465, L59
Errani R., Peñarrubia J., Walker M. G., 2018, MNRAS, 481, 5073
Evans N. W., Sanders J. L., Geringer-Sameth A., 2016, Phys. Rev. D, 93, 103512
Fitts A. et al., 2017, MNRAS, 471, 3547
Foreman-Mackey D., Hogg D. W., Lang D., Goodman J., 2013, PASP, 125, 306
Fritz T. K., Battaglia G., Pawlowski M. S., Kallivayalil N., van der Marel R., Sohn S. T., Brook C., Besla G., 2018, A&A, 619, A103
Gaia Collaboration, 2016a, A&A, 595, A1
Gaia Collaboration, 2016b, A&A, 595, A2
Gaia Collaboration, 2018b, A&A, 616, A12
Gaia Collaboration et al., 2018a, A&A, 616, A1
Gaia Collaboration et al., 2019, A&A, 623, A110
Garrison-Kimmel S. et al., 2018, MNRAS, 481, 4133
Geringer-Sameth A., Koushiappas S. M., 2011, Phys. Rev. Lett., 107, 241303
Geringer-Sameth A., Koushiappas S. M., Walker M., 2015b, ApJ, 801, 74
Geringer-Sameth A., Koushiappas S. M., Walker M. G., 2015a, Phys. Rev. D, 91, 083535
Geweke J., In F., Evaluating the Accuracy of Sampling-Based Approaches to the Calculation of Posterior Moments, 1995, 4
Gnedin O. Y., Kravtsov A. V., Klypin A. A., Nagai D., 2004, ApJ, 616, 16
González-Samaniego A., Bullock J. S., Boylan-Kolchin M., Fitts A., Elbert O. D., Hopkins P. F., Kereš D., Faucher-Giguère C.-A., 2017, MNRAS, 472, 4786
Goodman J., Weare J., 2010, Comm. App. Math. Comp. Sci., 5, 65
Grillmair C. J., 2009, ApJ, 693, 1118
Harbeck D. et al., 2001, AJ, 122, 3092
Harris W. E., 2010, preprint (arXiv:1012.3224)
Henden A. A., Levine S., Terrell D., Welch D., 2015, AAS, 225, 336.16
Hogan C. J., Dalcanton J. J., 2000, Phys. Rev. D, 62, 063511
Holl B. et al., 2018, A&A, 618, A30
Homma D. et al., 2016, ApJ, 832, 21
Homma D. et al., 2018, PASJ, 70, S18
Hormann K., 2014, in Approximation Theory XIV: San Antonio 2013. Springer, p. 197
Hui L., Ostriker J. P., Tremaine S., Witten E., 2017, Phys. Rev. D, 95, 043541
Husser T.-O., Wende-von Berg S., Dreizler S., Homeier D., Reiners A., Barman T., Hauschildt P. H., 2013, A&A, 553, A6
Hu W., Barkana R., Gruzinov A., 2000, Phys. Rev. Lett., 85, 1158
Iorio G., Belokurov V., 2019, MNRAS, 482, 3868
Jethwa P., Erkal D., Belokurov V., 2016, MNRAS, 461, 2212
Jethwa P., Erkal D., Belokurov V., 2018, MNRAS, 473, 2060
Joo S.-J. et al., 2018, ApJ, 861, 23
Kaplinghat M., Strigari L. E., 2008, ApJ, 682, L93
Kim D., Jerjen H., 2015, ApJ, 799, 73
Kim D., Jerjen H., Mackey D., Da Costa G. S., Milone A. P., 2016a, ApJ, 820, 119
Kim D., Jerjen H., Milone A. P., Mackey D., Da Costa G. S., 2015, ApJ, 803, 63
Kim D. et al., 2016b, ApJ, 833, 16
Kirby E. N., Cohen J. G., Guhathakurta P., Cheng L., Bullock J. S., Gallazzi A., 2013, ApJ, 779, 102
Kirby E. N., Cohen J. G., Simon J. D., Guhathakurta P., Thygesen A. O., Duggan G. E., 2017b, ApJ, 838, 83
Kirby E. N., Rizzi L., Held E. V., Cohen J. G., Cole A. A., Manning E. M., Skillman E. D., Weisz D. R., 2017a, ApJ, 834, 9
Kirby E. N., Simon J. D., Cohen J. G., 2015, ApJ, 810, 56
Kirby E. N. et al., 2010, ApJS, 191, 352
Koch A., Grebel E. K., Wyse R. F. G., Kleyna J. T., Wilkinson M. I., Harbeck D. R., Gilmore G. F., Evans N. W., 2006, AJ, 131, 895
Koleva M., Prugniel P., Bouchard A., Wu Y., 2009, A&A, 501, 1269
Koposov S. E., Belokurov V., Torrealba G., 2017, MNRAS, 470, 2702
Koposov S. E., Belokurov V., Torrealba G., Evans N. W., 2015a, ApJ, 805, 130
Koposov S. E. et al., 2011, ApJ, 736, 146
Koposov S. E. et al., 2015b, ApJ, 811, 62
Koposov S. E. et al., 2018, MNRAS, 479, 5343
Kraan-Korteweg R. C., Lahav O., 2000, A&AR, 10, 211
Kravtsov A. V., 2013, ApJ, 764, L31
Laevens B. P. M. et al., 2015, ApJ, 813, 44
Li T. S. et al., 2017, ApJ, 838, 8
Li T. S. et al., 2018, ApJ, 857, 145
Luque E. et al., 2016, MNRAS, 458, 603
Luque E. et al., 2017, MNRAS, 468, 97
Luque E. et al., 2018, MNRAS, 478, 2006
Madau P., Shen S., Governato F., 2014, ApJ, 789, L17
Malhan K., Ibata R. A., Martin N. F., 2018, MNRAS, 481, 3442
Martin N. F. et al., 2016a, ApJ, 830, L10
Martin N. F. et al., 2016b, ApJ, 833, 167
Mashchenko S., Wadsley J., Couchman H. M. P., 2008, Science, 319, 174
Mateo M. L., 1998, ARA&A, 36, 435
McConnachie A. W., 2012, AJ, 144, 4
McConnachie A. W. et al., 2008, ApJ, 688, 1009
McMillan P. J., 2017, MNRAS, 465, 76
Merritt D., Meylan G., Mayor M., 1997, AJ, 114, 1074
Monelli M. et al., 2018, MNRAS, 479, 4279
Moore B., 1994, Nature, 370, 629
Muñoz R. R., Geha M., Côté P., Vargas L. C., Santana F. A., Stetson P., Simon J. D., Djorgovski S. G., 2012, ApJ, 753, L15
Navarro J. F., Eke V. R., Frenk C. S., 1996a, MNRAS, 283, L72
Navarro J. F., Frenk C. S., White S. D. M., 1996b, ApJ, 462, 563
Navarro J. F., Frenk C. S., White S. D. M., 1997, ApJ, 490, 493
Nidever D. L., Dey A., Olsen K., Ridgway S., Fitzpatrick M., Scott A., 2018, AJ, 156, 131
Okamoto T., Frenk C. S., 2009, MNRAS, 399, L174
Peebles P. J. E., 2000, ApJ, 534, L127
Peñarrubia J., McConnachie A. W., Navarro J. F., 2008a, ApJ, 672, 904
Peñarrubia J., Navarro J. F., McConnachie A. W., 2008b, ApJ, 673, 226
Peñarrubia J., Pontzen A., Walker M. G., Koposov S. E., 2012, ApJ, 759, L42
Pontzen A., Governato F., 2012, MNRAS, 421, 3464
Read J. I., Agertz O., Collins M. L. M., 2016, MNRAS, 459, 2573
Read J. I., Gilmore G., 2005, MNRAS, 356, 107
Read J. I., Walker M. G., Steger P., 2018, MNRAS, 481, 860
Sanders J. L., Evans N. W., Dehnen W., 2018, MNRAS, 478, 3879
Schive H.-Y., Chiueh T., Broadhurst T., 2014, Nat. Phys., 10, 496
Schive H.-Y., Chiueh T., Broadhurst T., Huang K.-W., 2016, ApJ, 818, 89

Schlafly E. F., Finkbeiner D. P., 2011, ApJ, 737, 103
Schlegel D. J., Finkbeiner D. P., Davis M., 1998, ApJ, 500, 525
Schönrich R., Binney J., Dehnen W., 2010, MNRAS, 403, 1829
Sesar B. et al., 2014, ApJ, 793, 135
Shapley H., 1961, Galaxies
Sharp R. et al., 2006, in McLean I. S., Iye M., eds, Proc. SPIE Conf. Ser. Vol. 6269, Ground-based and Airborne Instrumentation for Astronomy. SPIE, Bellingham, p. 62690G
Simon J. D. et al., 2017, ApJ, 838, 11
Spencer M. E., Mateo M., Walker M. G., Olszewski E. W., McConnachie A. W., Kirby E. N., Koch A., 2017, AJ, 153, 254
Spergel D. N., Steinhardt P. J., 2000, Phys. Rev. Lett., 84, 3760
Tollet E. et al., 2016, MNRAS, 456, 3542
Torrealba G., Belokurov V., Koposov S. E., 2019, MNRAS, 484, 2181
Torrealba G., Koposov S. E., Belokurov V., Irwin M., 2016a, MNRAS, 459, 2370
Torrealba G. et al., 2016b, MNRAS, 463, 712
Torrealba G. et al., 2018, MNRAS, 475, 5085
Tulin S., Yu H.-B., 2018, Phys. Rep., 730, 1
van der Marel R. P., Guhathakurta P., 2008, ApJ, 678, 187
van Dokkum P. G., Abraham R., Merritt A., Zhang J., Geha M., Conroy C., 2015, ApJ, 798, L45
Vasiliev E., 2019, MNRAS, 484, 2832
Walker M. G., Mateo M., Olszewski E. W., 2008, ApJ, 688, L75
Walker M. G., Mateo M., Olszewski E. W., Bernstein R., Wang X., Woodroofe M., 2006, AJ, 131, 2114
Walker M. G., Mateo M., Olszewski E. W., Peñarrubia J., Wyn Evans N., Gilmore G., 2009, ApJ, 704, 1274
Walker M. G., Olszewski E. W., Mateo M., 2015, MNRAS, 448, 2717
Walker M. G., Peñarrubia J., 2011, ApJ, 742, 20
Walker M. G. et al., 2016, ApJ, 819, 53
Watkins L. L., van der Marel R. P., Sohn S. T., Evans N. W., 2019, ApJ, 873, 118
Weisz D. R. et al., 2016, ApJ, 822, 32
Wetzel A. R., Nagai D., 2015, ApJ, 808, 40
Whiting A. B., Irwin M. J., Hau G. K. T., 1997, AJ, 114, 996
Williams A. A., Belokurov V., Casey A. R., Evans N. W., 2017, MNRAS, 468, 2359
Zolotov A. et al., 2012, ApJ, 761, 71

This paper has been typeset from a TEX/LATEX file prepared by the author.